THE JOURNAL OF PHYSICAL CHEMISTRY B
A JOURNAL OF THE AMERICAN CHEMICAL SOCIETY

pubs.acs.org/JPCB

Featured Article

Exploring Biological Quantum Effects in Photosynthesis across Varied Spatial Scales

Meixia Ruan and Yuxiang Weng*

Cite This: *J. Phys. Chem. B* 2026, 130, 4017−4040

Read Online

ACCESS | Metrics & More | Article Recommendations

ABSTRACT: The utilization of quantum effects by nature to enhance photosynthetic efficiency has emerged as a subject of intense scientific inquiry. However, fundamental questions remain unresolved, most notably, whether coherent energy transfer occurs in the primary photochemical events. This featured article summarizes recent work from our group and collaborators, addressing several manifestations of biological quantum effects in photosynthesis across varied spatial scales. These include: (1) Coherent energy transfer in allophycocyanin (inter-pigment distance of 21 Å) and phycoerythrin 545 (15 Å). An exciton-vibrational coherence time of up to 500 fs and a 220 fs coherent energy transfer time have been observed in allophycocyanin. In contrast, in the structurally similar phycocyanin 620, which possesses an identical pigment pair and separation distance, energy transfer follows an incoherent way with a time constant of 460 fs. (2) Quantum switch in the light-harvesting complex of photosystem II of higher plants, which is driven by a dynamical protein structure. The antenna reversibly regulates light harvesting (Förster energy transfer, classical) and excess energy dissipation (Dexter energy transfer, quantum mechanical) states in response to dynamic changes in sunlight intensity. This switch is achieved by dynamic modulation of the distance between the main quenching pair, lutein 1 and chlorophyll *a* 612 (∼5.6 to 6 Å). (3) Macroscale quantum design in membrane architecture. The optimal size of intracytoplasmic membrane vesicles is regulated by quantum design principles in the LH2 structure, where the structural robustness and excitonic coherence of LH2 are preserved only within an evolutionarily optimized vesicle size range (50−80 nm).

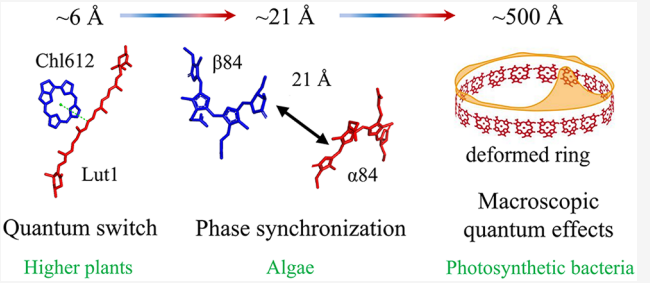

1. INTRODUCTION

Photosynthesis sustains life on earth by converting solar radiation into chemical energy. In photosynthetic organisms, pigment-binding complexes capture sunlight and transfer excitation energy to reaction centers for charge separation which initiates biochemical reactions.[1,2] These light-harvesting processes exhibit remarkably high quantum efficiencies, typically exceeding 95%,[2] making the underlying design principles a topic of considerable research interest. Advances in structural biology and ultrafast spectroscopy have extended spatial resolution to the Ångström scale and temporal resolution to the femtosecond regime. Consequently, studies of pigment-binding complexes have increasingly shifted from static structural descriptions toward dynamic, functionally relevant architectures and from classical statistical frameworks toward fully quantum-mechanical treatments.[3−5] The outstanding efficiency of natural light-harvesting systems relies on ultrafast excited-state dynamics, particularly excitation energy transfer (EET) and charge separation processes, in which quantum superposition and coherence play essential roles. Consequently, photosynthetic light harvesting has emerged as a paradigmatic model for exploring quantum effects in biological systems.[6]

At low light intensities, photosynthetic light-harvesting complexes transfer absorbed energy to the reaction center primary donor with a near-perfect quantum efficiency. Quantum coherence enables delocalized excitations to bypass local energy minima on the large and rugged energy landscape of the photosynthetic system. In an incoherent hopping picture, the excitation must dwell at each minimum and await a slow, thermally activated transfer step, whereas quantum coherence allows the excitation to "fly over" such energetic traps or to explore alternative pathways.[7] This coherence, rooted in quantum-mechanical superposition, can channel energy more directly toward the reaction center, thereby reducing dissipative losses and enhancing the overall quantum yield. The prospect that nature utilizes quantum coherence to optimize such a fundamental biochemical process challenges

Received: October 25, 2025
Revised: March 19, 2026
Accepted: March 20, 2026
Published: April 1, 2026

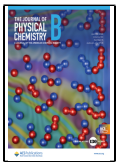

https://doi.org/10.1021/acs.jpcb.5c07333
J. Phys. Chem. B 2026, 130, 4017−4040

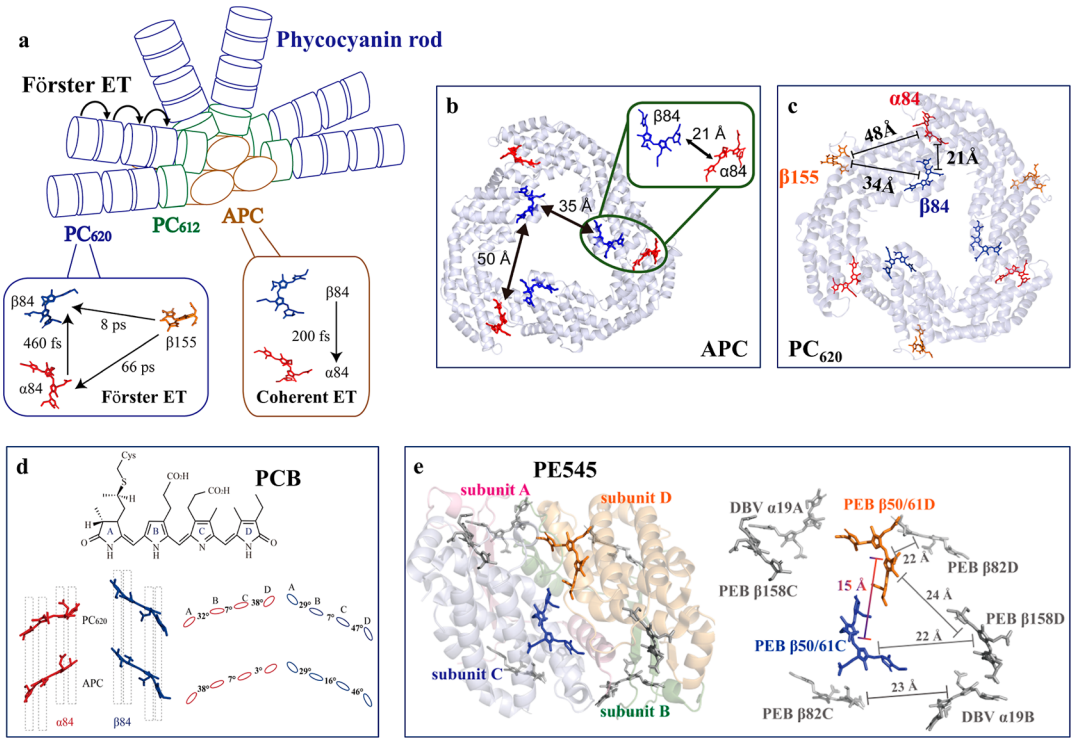

Figure 1. (a) Model for the PBS, with hexametric PC_{620} in the rods and APC in the core.[14] (b) Crystal structure of APC with the β (blue) and α (red) PCB pigments (PDB ID: 1ALL). In the trimer, a β-pigment is close to the α-pigment of a neighboring monomer with an electronic coupling of about 155 cm^{-1}.[15] (c) X-ray structure of the PC_{620} trimer with the β84 (blue), β155 (orange), and α84 (red) PCB pigments (PDB ID: 1I7Y).[14] (d) Upper panel: structure of the PCB pigment. Lower panel: comparison of the PCB pigment structure in PC_{620} and APC. (e) Left: X-ray structure of dimeric PE545 from cryptomonad *Rhodomonas* CS24 (PDB ID: 1XF6) with the four subunits (A–D) shown in pink (α), green (α), blue (β), and orange (β). Right: the distribution of the pigments in PE545 with the labeled distances between them. The coupled pigment pairs PEB β50/61C and PEB β50/61D with the shortest distance of 15 Å are plotted in blue and orange, respectively.[19] (a, c) Reprint with permission from ref 14. Copyright 2024 AIP Publishing. (b) Reprint with permission from ref 15. Available under a CC-BY license. Copyright 2024 Ruidan Zhu et al. (e) Reprint with permission from ref 19. Copyright 2025 AIP Publishing.

the long-standing view that decoherence in warm, wet, and noisy biological environments precludes any functional quantum effects.[8] In such environments, thermal fluctuations ($\sim kT$) are orders of magnitude larger than the subtle quantum energy scales, and nuclear vibrations are insensitive to the transitions occurring around them, so that any coherence would therefore be expected to be "washed out".[6]

In a recent low-temperature (7 K) high-vacuum experiment using a synthetic donor–acceptor pair, Kong et al. constructed both a coherent EET pathway and a classical hopping pathway.[9] They found that the coherent EET efficiency was three times that of the hopping mechanism. This striking enhancement, however, has not yet been directly observed in natural photosynthetic systems.[9] Then, what constitutes uniquely "quantum" effects in biology? What constitutes "nontrivial quantum effects" that could serve as the origin of observable biological quantum phenomena?[10] At the molecular level, all processes from bond formation to electronic state excitation or dissipation, as well as vibrational and rotational motions, are governed by quantum mechanics. Consequently, phenomena that can be directly attributed to single-molecule properties, such as the absorption or emission spectra of pigments, fall outside the scope of quantum biology. Instead, the microscopic characteristics of quantum biology should involve cross-molecular phenomena, where molecular wave functions exhibit delocalized properties. Thus, models based on quantum theory are crucial for understanding the primary processes of photosynthesis. In this article, we define biologically functional quantum effects as phenomena that (i) rely on coherent or nonclassical correlations extending over more than one chromophore, (ii) persist on time scales comparable to biological function, and (iii) measurably alter the efficiency, regulation, or robustness of the system. Excitons are inherently quantum superpositions of multiple molecular excited states within a complex. Consequently, photon absorption in a light-harvesting complex generates collective excitation in the complex. The observed coherence decays through two primary mechanisms. The first is ensemble dephasing, which does not destroy coherence within individual complexes but disrupts the correlation between the oscillatory behavior of individual members of the ensemble, leading to the loss of measurable oscillatory signals. The second is microscopic dephasing (or decoherence), which destroys coherent superpositions between excitons within a single complex.[7] Given the inherent fragility of quantum effects in delocalized molecules, environmental perturbations affect quantum properties in both time (coherence lifetime) and space (delocalization length). Studies indicate that the decoherence time for excitons in photosynthetic complexes at room temperature is typically about tens of femtoseconds, which mismatches the hundreds of femtoseconds required for the EET.[11,12] Whether such coherence provides functional advantages to the photosynthetic apparatus remains a debate,[10] which casts the doubts on the existence of the coherent EET mechanism in the primary photosynthetic process.[13] Therefore, to explore the biological quantum effects in photosynthesis, several key issues

https://doi.org/10.1021/acs.jpcb.5c07333
J. Phys. Chem. B 2026, 130, 4017–4040

must be addressed: (1) How can excitons overcome the environmental noise to sustain coherence on a time scale comparable to the EET time? (2) Can the protein structure dynamically regulate quantum effects to enhance biological function? (3) Can biological quantum effects extend beyond the nanoscale, yielding observable quantum phenomena at cellular levels comparable to those at microscopic scales?

The delocalization of excitation energy among pigment molecules is a key signature of quantum effects in primary photosynthetic processes. Depending on the microscopic spatial scale and the specific light-harvesting complex, these quantum effects can manifest in diverse ways, which are closely linked to distinct biological functions. In this perspective, we review biologically relevant quantum effects in photosynthesis occurring at spatial scales ranging from about 5.6 to 500 Å, based primarily on recent works from our group and collaborators as follows:

- The respective coherent and incoherent EET mechanisms of the light-harvesting complexes allophycocyanin (APC) and phycocyanin 620 (PC_{620}) from *Thermosynechococcus Vulcanus*, located in the phycobilisomes (PBS), together with coherent EET in phycoerythrin 545 (PE545) in cryptophyte algae, at a spatial scale of ∼15 to 21 Å. The corresponding protein structures are shown in Figure 1. APC is an integral component of the light-harvesting antenna in blue and red algae, capable of delivering the energy absorbed from the PBS rods to the reaction center (RC). PC_{620}, also known as C-phycocyanin (CPC), forms the outermost light-harvesting antenna in the PBS rod and is responsible for light harvesting and EET to APC.[14]

Coherent EET is observed in APC, which contains three identical phycocyanobilin (PCB) pigment pairs (α84−β84). The EET time from the upper to the lower excitonic level is 220 fs, while the long-lived exciton-vibrational coherence persists for approximately 500 fs. This long coherence is achieved in a dimeric exciton model through quantum phase synchronization, driven by exciton-vibrational energy dissipation. The long-lived coherence exhibits an inherent capacity to protect itself against environmental noise, which is realized by dissipating the fast-dephasing, resonant antisymmetric collective vibrational modes coupled to the excitonic levels. Consequently, only the non-dissipative correlated symmetric modes remain.[15] PC_{620} possesses a structure that is essentially identical to APC, with its three α84−β84 PCB pairs occupying nearly the same spatial positions (Figure 1b,c). Despite this structural similarity, EET from α84 to adjacent β84 in PC_{620} is incoherent, with a time constant of 460 fs. The pronounced difference in the EET mechanism, i.e., coherent in APC versus incoherent in PC_{620}, can be attributed to a subtle twist of the α84 in PC_{620} (Figure 1d, lower panel) and site energy difference.

- Quantum switch reversibly regulating light harvesting and excess energy dissipation in the photosynthesis of high plants operates at an ∼6 Å spatial scale. The major light-harvesting complex of photosystem II (LHCII) is known to switch between two states of different functions, i.e., it transfers absorbed energy to the reaction center with near-unit efficiency under low light, whereas under high light, it dissipates damaging excess energy as heat, a process known as non-photochemical quenching (NPQ). However, the molecular-level mechanism underlying this two-state transition has remained elusive. By integrating single-particle cryo-electron microscopy (cryo-EM) studies of LHCII dynamic structures at atomic resolution, multi-state density functional theory (MSDFT) calculations of the coupling strength between the key quenching pair lutein 1 (Lut1)−chlorophyll *a* 612 (Chl612), and transient fluorescence experiment, a significant quantum switch mechanism in LHCII has been revealed with Lut1-Chl612 distance as the critical control parameter. This distance, modulated by lateral pressure on LHCII and associated conformational changes, regulates the EET channel by tunning a slight change at its critical distance of 5.6 Å, enabling reversible switch between light harvesting and excess energy dissipation. In this case, nature exploits the advantages of quantum effects as follows: at low light intensities, when the Lut1−Chl612 distance is ∼6.0 Å, excitation energy is transferred from the S_2 state of lutein to the Q_y state of Chl*a* via the Förster resonance energy transfer (FRET) mechanism. While at high light intensities, when the Lut1−Chl612 distance is shorter than 5.6 Å (the van der Waals contact distance), the energy transfer direction reverses, i.e., excess excitation energy in the Q_y state of Chl*a* is quenched by the S_1(dark) state of Lut1 through a Dexter energy transfer quantum mechanism and ultimately dissipated as heat.[16,17]
- Macroscale optimal size of the intracytoplasmic membrane (ICM) vesicles (∼500 Å) is regulated by the quantum design principle in the light-harvesting antenna complex 2 (LH2) structure. Photosynthetic bacterial LH2 adopts a flat disc conformation, composed of ring-like bacteriochlorophylls (Bchl) aggregates that form an excitonically optimal structure following the quantum mechanical principle for efficient EET. We find that the stiffness and robustness of this quantum-optimized LH2 structure ensure efficient EET even under varying environmental conditions, including membrane curvature. At the optimal vesicle size of approximately 50−80 nm, LH2 restores its flat disc form on the curved membrane. The maintenance of this exceptional structural design illustrates how design principles originated from quantum-optimized molecular architectures can propagate across organizational scales, from the sub-10 nm LH2 protein complex to 50 nm membrane vesicles.[18]

2. COHERENT EET IN LIGHT-HARVESTING COMPLEXES

2.1. Excitonic Coherences Alone Cannot be the Origin of the Observed Long-Lived Coherence

Extensive research has been motivated by the hypothesis that nature utilizes quantum coherences to enable efficient EET within light-harvesting complexes. Initially, the coherences were regarded as excitonic.[20−24] Nowadays, the understanding has shifted toward a vibronic coupling model.[25−29] Current evidence strongly indicates that coherent exciton-vibrational dynamics, which originates from non-adiabatic transitions between excited states, can persist over long time scales (typically picoseconds) at room temperature.[1,30−32] Previous literature studies employed various related terms, such as "exciton-vibrational coupling", "vibronically mixed excited

https://doi.org/10.1021/acs.jpcb.5c07333
J. Phys. Chem. B 2026, 130, 4017−4040

states", "vibronic excitons", or "vibronic exciton states".[33−37] These all describe excitonically mixed electronic and vibrational states that involve at least two interacting chromophores. In contrast, a vibronic state typically refers to the excited electronic state of a single molecular concomitant with its own vibrational manifold.[38,39] To distinguish between coherences that arise from the excited-state manifold and those from the ground-state manifold, the term vibrational coherence is reserved for wave packet contribution (in either the ground or excited state) within a monomer. For coherences in the excited-state manifold of a dimer that involve significant vibrational character, the terms vibronic coherence, or more specifically, vibronic-exciton coherences are employed.[35,40]

Quantum coherence, arising from the superposition of excitonic states (mathematically represented by off-diagonal elements in the density matrix),[10] can be experimentally detected as quantum beats in EET dynamics. Consequently, these quantum beats, lasting several hundred femtoseconds, have been regarded as signatures of quantum EET in photosynthetic antenna systems. This wave-like EET mechanism can contribute to the near-perfect quantum efficiency of photosynthesis only if coherences survive during EET under physiological conditions. As temperature rises, thermally activated vibrational modes of the protein bath induce larger energy fluctuations, thereby accelerating decoherence.[41,42] Although this dephasing seems unfavorable, Mohseni et al.[43] and Plenio and Huelga[37] have independently demonstrated that a delicate interplay between quantum coherence and dephasing can create fast, unidirectional transfer pathways within these complexes, thereby enhancing electronic EET efficiency.[44−46] This scheme exploits quantum coherence to overcome energy barriers, but subsequent dephasing processes trap the excitation at the target site. Thus, optimal energy transport requires both dephasing and coherent EET.[47]

Long-lived coherences in spectroscopic signals have been observed in various light-harvesting complexes at room temperature.[19,22,48,49] Over the past decades, intense research has focused on quantum coherence EET in the Fenna−Matthews−Olson (FMO) complex, a light-harvesting antenna purified from the green sulfur bacterium *Chlorobaculum tepidum*.[11,15,21,23,50,51] Numerous studies have proposed such "environmental protection of excitonic coherence" as the source of long-lived oscillations in 2D spectra.[10,52−54] However, quantum mechanics/molecular mechanics dynamical simulations of FMO have not identified correlations in site energy fluctuations.[10,55,56] Both the mixed quantum-classical and fully quantum descriptions indicate that dephasing of inter-exciton coherences typically results in sub-100 fs decay times at room temperature, substantially shorter than the inter-complex EET times and thus unlikely to play a functional role. Quantum coherences in FMO complexes have become the center of debate because of their paradigmatic status in quantum biology. Recent two-dimensional electronic spectroscopy (2DES) experimental studies of this complex suggest that the observed long-lived quantum beats are inconsistent with inter-exciton coherence.[11,50,57] Instead, these oscillations mostly reflect characteristics of Raman-active vibrational modes on the electronic ground-state surface with some contribution from the excited-state vibrational coherences, unrelated to the EET process. For a more detailed discussion, see the excellent review by Cao et al.[10] Recent work further indicates that considerably more complicated dynamics may appear when vibrational and electronic energy gaps are in resonance. Such resonances lead to inseparability of nuclear and electronic degrees of freedom,[58,59] which some theoretical studies suggest may influence EET.[48]

It was realized that the observed long-lived coherences may be neither electronic nor vibrational but a mixture of the two, termed "vibronic" coherence. Coupling of electronic transitions with underdamped vibrational modes may result in inter-exciton coherences with strong intrapigment character, that is, consisting of wave packets on different vibrational levels of the same chromophore.[36] Christensson et al. proposed a vibronic exciton model to explain the long-lived oscillations observed in FMO. This description of "vibronic" coherence arises from the coupled chromophores and should be distinguished from localized vibrational coherences within a single, uncoupled excited state manifold.[59] It has been further demonstrated that, under conditions of weak excitonic and vibronic coupling, the conservation of coherence works optimally through mixing with vibrational degrees of freedom when the vibrational quantum is resonant with the electronic energy splitting.[40] Tiwari and Jonas proposed a non-adiabatic vibrational-electronic mixing model in which such mixing enhances the stimulated Raman excitation of the resonant delocalized vibrations in the ground state. This model predicted that the observed coherences could originate from the ground state.[58,60] Although long-lived coherence signatures are repeatedly observed in the spectroscopic signals from biological systems, their origin remains contentious because it is unclear how these systems avoid decoherence induced by interactions with noisy environments. Lim et al. provided experimental and theoretical evidence that coherent exciton-vibrational (vibronic) coupling underlies the long-lived coherence (up to 800 fs) observed in an artificial light-harvesting system, a molecular J-aggregate. Their analysis further revealed that the long-lived oscillatory signals are dominated by excited-state coherence rather than ground-state coherence. Experimentally, the pure vibrational coherence and exciton-vibrational coherence can be distinguished by double cross (DC) polarization 2DES.[11,61,62]

It should be noted that in previous investigations of coherent EET in a light-harvesting complex other than FMO, i.e., APC, a protein located at the base of the PBS of cyanobacteria, vibronic coupling was identified as a key factor governing the EET dynamics by Womick and Moran. They showed that a vibronic exciton model predicts the experimental EET rate more accurately than a purely excitonic model, where the vibronic coupling both broadens the absorption line shape and opens channels for fast internal conversion of the excited energy at the upper excitonic level.[48,49] More recently, Sohoni et al. reported that two low-frequency vibrations in CPC of the PBS are nearly resonant with the inter-excitonic energy gap, resulting a several-fold enhancement of the inter-exciton EET rate at room temperature.[63]

A straightforward view of how vibrational motion modulates quantum beating between the two excited states (S_1 and S_2) was provided by Freixa et al. Their non-adiabatic excited state molecular dynamics (MD) simulations on a rigid synthetic heterodimer revealed ultrafast beating of S_1 and S_2 electronic populations at room temperature. These oscillations are vibrationally assisted and are not observed at low temperatures. The observed persistent non-adiabatic transitions between excited states funnel the EET through specific vibrational motions that in turn modulate the quantum beating between the electronic excited states. Moreover, vibrations whose

https://doi.org/10.1021/acs.jpcb.5c07333
J. Phys. Chem. B 2026, 130, 4017−4040

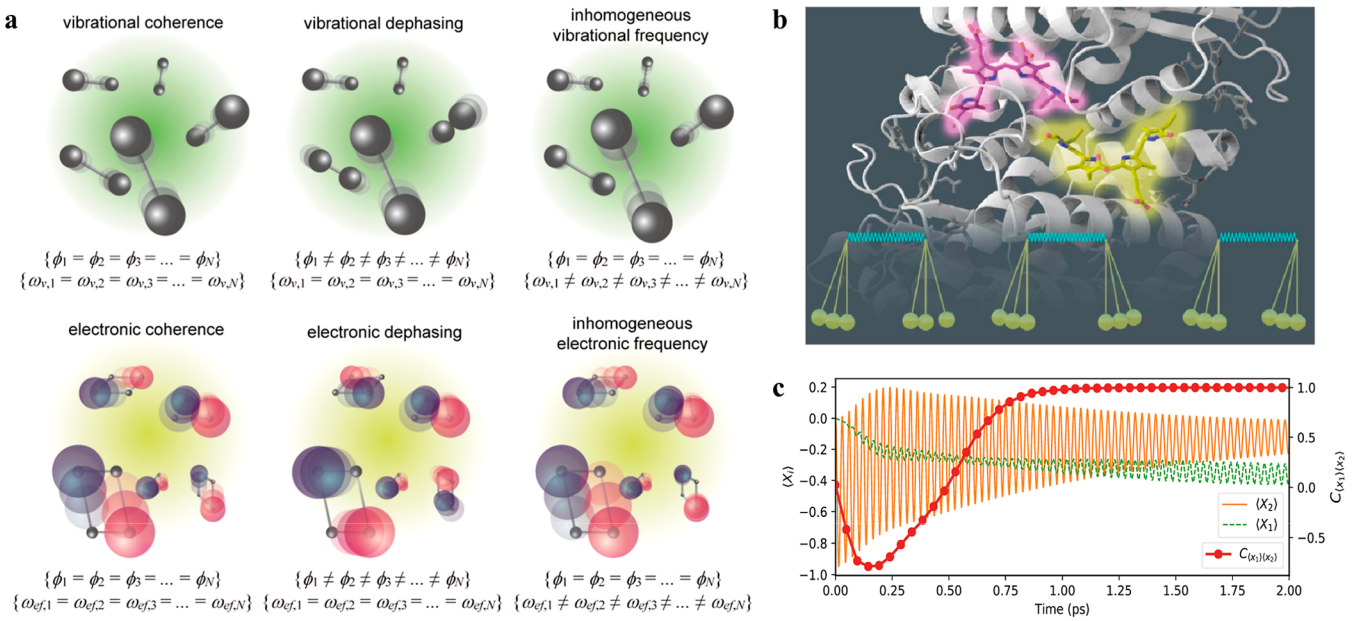

Figure 2. (a) Schematic illustration of vibrational (upper) and electronic (lower) coherences (left), dephasing (middle), and decoherence (right) induced by environmental noises in the condensed phase. ϕ and ω_v refer to the phase and frequency, respectively, of each oscillator, and ω_{ef} refers to the transition frequency between the initial and final electronic states.[33] (b) Illustration of the central weakly interacting chromophore pair in the light-harvesting protein phycoerythrin 545. The pendulum illustrates local vibrations, which are involved in energy transfer.[66] (c) The associated symmetric collective vibrational motion undergoes slow dissipation, leading to positive quantum phase synchronization of local vibrational displacements (the correlation function $C_{<X1><X2>} \sim 1$, where 1 indicates fully positively synchronized) in the picosecond time regime.[68] (a) Reproduced with permission from ref 33. Copyright 2022 American Chemical Society. (b) Reproduced with permission from ref 66. Copyright 2025 American Chemical Society. (c) Reproduced with permission from ref 68. Copyright 2019 Royal Society of Chemistry.

frequencies match the electronic population beating period contribute most strongly to the $S_1 \rightarrow S_2$ electronic transitions. That is, excess electronic energy flows into vibrations in the presence of strong electron−phonon coupling, creating specific vibrational excitations that ultimately modulate the electronic quantum beating.[64] This model resembles an earlier proposed mechanism by Chin et al., which describes a novel type of coherence generation and storage process driven by vibrational modes. In that model, electronic coherences are assumed to arise from resonant coupling with robust vibrational coherences. The constant transfer from the long-lived vibrational coherences is assumed to maintain long-lived oscillations on the otherwise fast dephasing electronic coherences.[65]

2.2. Model of Resonant Exciton-Vibrational Coupling of the Collective Modes

Consider a vibronic excitation from the $v = 0$ electronic ground state to multiple vibrational levels of an electronic excited state.[48] The coefficient of each vibrational state is determined by the corresponding Franck−Condon factor, and the superposed wave function results in a wave packet localized at the equilibrium position of the ground state. A vibrational wave packet describes classical molecular vibration (Figure 2a, upper panel). In contrast, an electronic wave packet represents a superposition of electronic states in the molecule (Figure 2a, lower panel). In the condensed phases and at ambient temperature, however, individual molecular wave functions do not evolve in lockstep because of randomized environmental orientation and energetic disorder. Randomized environmental orientation disperses the phase ϕ of each wave function through the system−environment interaction (middle column in Figure 2a), while the energetic disorder leads to a distribution of oscillation frequencies ω (right column in Figure 2a).[66] As a result, interaction with a noisy environment would lead to decoherence of either electronic or vibrational superposition states. Typical coherence times for chromophores in solution are on the order of tens of femtoseconds for electronic transitions and several picoseconds for vibrational transitions.[67]

Therefore, a critical question is how light-harvesting complexes or artificial systems can maintain long-lived quantum coherence despite interactions with noisy, fluctuating environments, specifically, what mechanisms they employ to protect against coherence loss.[65] Although spatially correlated environmental fluctuations of the protein-bound pigments have been proposed as a mechanism protecting the observed long-lived coherence.[52,69,70] Quantum mechanics/molecular mechanics dynamic studies of the FMO protein have not identified correlations in site energy fluctuations.[55,71] In a normal-mode analysis of the FMO spectral density, correlations were found but only at very low vibrational frequencies.[72] These correlations were calculated to have practically no influence on the populations of exciton states. Consequently, theoretical studies have shifted to coherence-protection mechanisms other than the "environmental protection of excitonic coherence". For example, Siwiak-Jaszek and Olaya-Castro proposed a model of transient synchronization in an exciton-vibrational coupled vibronic dimer.[66,68,73,74] This model showed that coherent energy transport coincides with the emergence of positive synchronization (in phase) between mode displacements, suggesting that coherence in biomolecules can promote the synchronization of vibrational motions driven by thermal equilibrium or environmental noise. Transient spontaneous synchronization can lead to very weak energy dissipation due to collective motion. In this framework, collective motions were treated as the projection of the

https://doi.org/10.1021/acs.jpcb.5c07333
J. Phys. Chem. B 2026, 130, 4017−4040

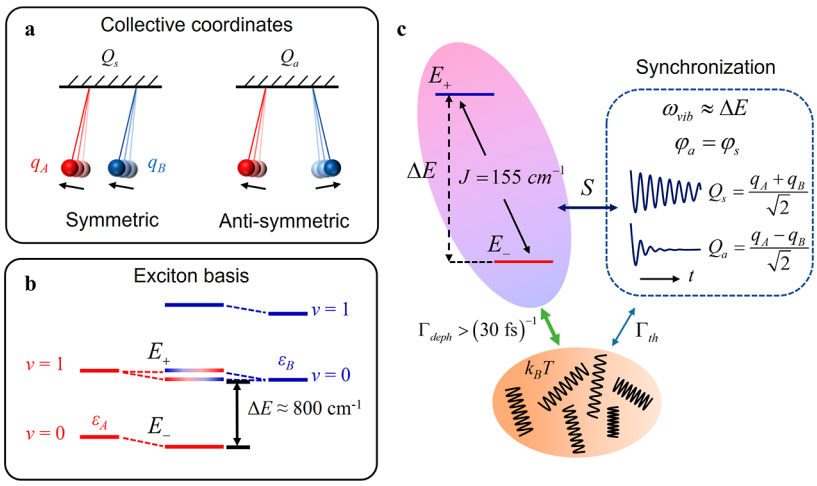

Figure 3. Mechanism of quantum phase synchronization. (a) Schematic diagram of symmetric (Q_s) and antisymmetric (Q_a) collective coordinates with reference to a pair of Huygens pendulums. q_A and q_B are localized intramolecular vibrational coordinates. (b) The energy diagram of the exciton-vibrational dimer. E_+ and E_- are the eigen energies of the two delocalized states under the exciton basis. (c) The mechanism of energy dissipation by the antisymmetric modes via coupling to the delocalized excitonic levels with a rate constant of Γ_{deph}; the symmetric modes undergo dephasing by coupling to the thermal bath with a rate constant of Γ_{th}.[15] (a–c) Reproduced with permission from ref 15. Available under a CC-BY license. Copyright 2024 Ruidan Zhu et al.

individual localized intramolecular vibrational coordinates into symmetric and antisymmetric collective vibrational coordinates (Figures 2b,c and 3a). It turns out that only the antisymmetric vibrations can be coupled to excitonic levels. Cho et al. performed simulation work on the vibronic dimer model and showed that the local underdamped vibrations in a dimeric pair, which are resonant with the electronic energy gap, are synchronized as the EET is completed.[75] Tiwari et al.[58] similarly noted that the anticorrelated vibrational component, which couples to the electronic state and induces energy-gap fluctuations, drives EET via non-adiabatic dynamics. The transient synchronization predicts that some molecular motions can undergo transient quantum phase synchronization mediated by exciton-vibrational coupling, while EET takes place. This is a quantum phenomenon in which a collective symmetric vibrational motion undergoes slow dissipation due to effective decoupling from the environment via exciton-vibration coupling.

The resonant exciton-vibrational coupling model for the $\alpha84-\beta84$ PCB excitonic dimer in the APC trimer is illustrated in Figure 3.[15] The model consists of a non-degenerate homodimer (with monomers designated as A and B). Each molecule has an identical intramolecular harmonic vibration of frequency ω, which is resonant with the excitonic energy gap ΔE. The corresponding Hamiltonian, including the ground state and two singly excited states (excitonic levels) in the local site basis, is given by[15,19]

$$\begin{aligned}\hat{H} &= T + [V_A(q_A) + V_B(q_B)]|g\rangle\langle g| \\ &+ [\varepsilon_A + V_A(q_A^*) + V_B(q_B)]|e_1\rangle\langle e_1| \\ &+ [\varepsilon_B + V_A(q_A) + V_B(q_B^*)]|e_2\rangle\langle e_2| \\ &+ J[|e_1\rangle\langle e_2| + |e_2\rangle\langle e_1|] \end{aligned} \tag{1.1}$$

where T is the kinetic energy, $V(q)$ is the potential energy surface, ε is the site energy, and q^* and q are the dimensionless coordinates of the excited and ground states for the two molecules, respectively, and they satisfy the equation of $qi^* = q_i + d_i$, where d_i is the dimensionless displacement of the nuclear coordinate for the excited state with respect to that of the ground state. $|g\rangle$ and $|e\rangle$ represent the ground and excited states on a local electronic wave function basis, respectively. The intramolecular vibrational modes are converted into two intermolecular collective modes, i.e., the symmetric collective component, $Q_s = (q_A+q_B)/\sqrt{2}$, and the antisymmetric collective component, $Q_a = (q_A-q_B)/\sqrt{2}$. Under weak electronic coupling (J) and a significant site energy difference ($\Delta = \varepsilon_A - \varepsilon_B$), $\Delta/2 \gg J$.

Thus, the electronic energy can be expressed as

$$\begin{aligned} E_+ &= (\varepsilon_A + \hbar\omega S) - \hbar\omega\sqrt{S}(Q_s^* - Q_a^*) \\ E_- &= (\varepsilon_B + \hbar\omega S) - \hbar\omega\sqrt{S}(Q_s^* + Q_a^*) \end{aligned} \tag{1.2}$$

where the subscripts $\pm$ indicate the upper and lower energy levels, respectively.

The motion for high-frequency molecular vibrational and local intermolecular modes as collective solvent motion was treated with a multimode Brownian oscillator model, assuming that each mode experiences Brownian motion with a time-dependent Langevin friction function, which represents the Gaussian stochastic random force due to solvent motion acting on the jth mode ($f_j(t)$).[76,77] We further assume that $f_j(t) = 0$, and for the vibrational modes of high frequencies, such as >500 cm^{-1}, the relaxation rate $\gamma \ll \omega_j$, then the nuclear motion for jth underdamped oscillation can be derived as

$$q(t) \approx A_0 e^{-\gamma_j t/2}\left(\cos(\omega_j t + \varphi_j) + \frac{\gamma_j}{2\omega_j}\sin(\omega_j t + \varphi_j)\right) \tag{1.3}$$

where φ is the initial phase and A_0 is the oscillation amplitude.[15]

The excited-state nuclear motion $q^*(t)$ takes the same form as that of $q(t)$. When a dimer is considered, eq 1.3 also applies to the motion of the collective modes. In the measurement of the time-dependent dynamical Stokes shift, generally, the

https://doi.org/10.1021/acs.jpcb.5c07333
J. Phys. Chem. B 2026, 130, 4017−4040

upper excitonic level (E_+) decays too fast to be measured, and we focus only on the lower energy level (E_-). The time-dependent term is

$$E_-(t) = -\hbar\omega\sqrt{S}\,(Q_s^*(t) + Q_a^*(t)) \tag{1.4}$$

in a weakly coupled excitonic dimer, taking the relaxation rates for the asymmetric and symmetric collective modes as $\gamma_s \approx \gamma_{as}$, the time-dependent dynamical Stokes shift of the lower excitonic energy level coupled to jth vibrational mode in terms of collective mode is given as

$$E_-^j(t) = -2A_0^*\sqrt{S_j}\,\hbar\omega_j e^{-\gamma_j^* t/2}\cos\left(\frac{\varphi_s^j - \varphi_a^j}{2}\right)\left[\cos\left(\omega_j t + \frac{\varphi_s^j + \varphi_a^j}{2}\right) + \frac{\gamma_j^*}{2\omega_j}\sin\left(\omega_j t + \frac{\varphi_s^j + \varphi_a^j}{2}\right)\right] \tag{1.5}$$

where φ_s^j and φ_{as}^j are the initial phases of the symmetric and antisymmetric collective modes, which can be uncorrelated initially in a weakly coupled dimer. When the antisymmetric and symmetric collective modes are synchronized, i.e., $\varphi_s^j - \varphi_{as}^j = \pi$, then we have $E_-^j(t) = 0$, which indicates that the synchronized vibrational modes would not participate in the electronic energy dissipation. It should be noted that in our earlier work,[15] a phase difference of π has been assigned to the antisymmetric and symmetric collective modes, leading to a phase synchronization condition of $\varphi_s^j - \varphi_{as}^j = 0$.

The coupling between the excitonic levels and the resonance vibrational modes can be illustrated by the delocalized excitonic basis. By using the corresponding Hamiltonian, the local electronic wave function basis is changed to the delocalized excitonic basis ($|E_i\rangle$) via a rotation operator $U(\theta)$[73]

$$\begin{pmatrix}|E_1\rangle\\ |E_2\rangle\end{pmatrix} = U^\dagger(\theta)\begin{pmatrix}|e_1\rangle\\ |e_2\rangle\end{pmatrix} \tag{1.6}$$

where $U(\theta) = \begin{pmatrix}\cos\theta & \sin\theta\\ -\sin\theta & \cos\theta\end{pmatrix}$. $\theta = \frac{1}{2}\arctan\left(\frac{2J}{\Delta}\right)$ is referred to as the mixing angle, which is an effective measure of delocalization of the electronic subsystem or the exciton size. Subsequently, the exciton-vibrational coupling Hamiltonian is

$$H_{coupling} = \hbar\omega\sqrt{S}\sin(2\theta)Q_a^*\sigma_x \tag{1.7}$$

where $\sigma_x = |E_1\rangle\langle E_2| + |E_2\rangle\langle E_1|$ is the transition operator.

Siwiak-Jaszek and Olaya-Castro used creation and annihilation operators to express the electron-vibrational interaction, with the Hamiltonian reading as

$$H_{el\text{-}vib} = g_1|e_1\rangle\langle e_1|(b_1 + b_1^\dagger) + g_2|e_2\rangle\langle e_2|(b_2 + b_2^\dagger) \tag{1.8}$$

where $b_n^\dagger$ and b_n are the bosonic create and annihilate operator, respectively[68,73,74] Under the condition that $\omega_1 = \omega_2$ and $g_1 = g_2 = g$, where g_i denotes the electronic-vibrational coupling strength, the exciton-vibration Hamiltonian can be expressed in terms of effective Pauli matrices for the excitonic system as

$$H_{el\text{-}vib} = \sqrt{2}\,g(\cos 2\theta\sigma_z + \sin 2\theta\sigma_x)Q_{as} \tag{1.9}$$

Thus, the electron-vibrational coupling term is $H_{el\text{-}vib} = \sqrt{2}\,g\sin 2\theta\sigma_x Q_{as}$. The result is the same as eq 1.7.

Obviously, only the antisymmetric collective modes can couple to the two delocalized excitonic states. Therefore, when these antisymmetric collective modes are in resonance with the two delocalized excitonic states, vibrational energy will be dissipated into the environment through fast excitonic dephasing (30 fs^{-1}), leaving only the correlated symmetric collective modes to persist. Since the resonant symmetric collective modes are decoupled from the excitonic states, they do not participate in the electronic energy dissipation process, which renders the excitonic dimer an effective mechanism for protecting vibrational coherence against environmental fluctuations. As a result, the resonant vibrational mode would not appear in the dynamic Stokes shift spectra. These provide three experimentally measurable criteria for verifying whether an observed long-lived coherence is the exciton-vibrational coherence in origin:

- Longer exciton-vibrational coherence lifetime in the excitonic dimer than that of the vibrational in the nonexcitonic system.
- Half-loss in Raman intensity for the near resonant coherent vibrational modes for strongly coupled pair, and significantly less for weak couplings.

For a strongly coupled excitonic pair, owing to the fast relaxation of the antisymmetric modes, only the decoupled symmetric collective modes are detected. Regarding the Raman intensity of ground-state modes, Tiwari et al. showed that during the resonance Raman excitation of the strongly coupled dimer, anticorrelated vibrational wave packets are in resonance with the electronic transition.[58] Thus, the anticorrelated collective modes are dominant in the ground state, leading to an expected half-loss in Raman intensity for a strongly coupled dimer. This aligns well with the model proposed by Jonas et al. based on Huang−Rhys factors for the collective modes.[78] According to their work, the Raman loss for the resonant modes is given by $(1-\cos^2(2\theta_d))/2$. For strong coupling ($\cos^2(2\theta_d) = 0$), the loss is 0.5, whereas for weak coupling ($\cos^2(2\theta_d) \approx 1$), it approaches zero.

- Absence of the nearly resonant vibrational modes in the dynamical Stokes shift coherence spectra for both weakly and strongly coupled systems.

2.3. Observation of Long-Lived Exciton-Vibrational Coherence via Quantum Phase Synchronization in a Relatively Strong Exciton-Vibration Coupling System of the APC Trimer

APC is an integral component of the light-harvesting antenna in blue and red algae, capable of delivering the energy absorbed from the PBS rods to RC with an overall quantum efficiency of over 90%.[79] In the APC trimer, PCB pigments on different monomers are positioned sufficiently close (~21 Å apart) to form three identical $\alpha84-\beta84$ dimers. EET between the excitonically coupled PCB pigments has been reported to occur on a time scale of 200−400 fs.[49,80−82] The energy splitting (ΔE = 800 cm^{-1}) between the upper and lower excitons of the $\alpha84-\beta84$ dimer in APC, which is determined from absorption and fluorescence spectra, is significantly larger than the electronic coupling (J = 155 cm^{-1}) measured by circular dichroism (CD) spectroscopy, leading to a site energy (ε) difference of $\Delta_s = \varepsilon_{\beta84} - \varepsilon_{\alpha84} = \sqrt{\Delta E^2 - (2J)^2} = 737 cm^{-1}$. The EET between the two excitonic levels in the trimer was measured by 2DES, yielding a time constant of 220 fs. Pronounced coherence signals were observed in the trimer, α-subunit, and monomer after the subtraction of the fitted decay envelopes

https://doi.org/10.1021/acs.jpcb.5c07333
J. Phys. Chem. B 2026, 130, 4017−4040

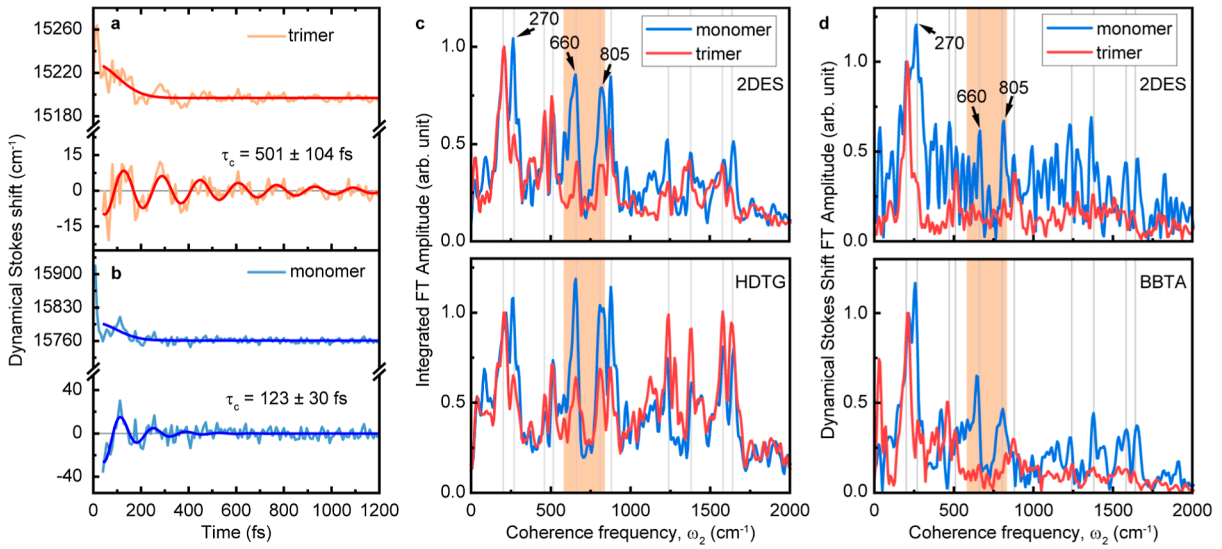

Figure 4. The long-lived coherence in the dynamical Stokes shift of the recombinant allophycocyanin (rAPC) trimer, and reduction in the Raman intensities of the resonant vibrational modes in the coherence spectra and the absence of the resonant mode in the dynamical Stokes shift spectra of the rAPC trimer. The dynamical Stokes shift of the diagonal peaks at 15,300 cm^{-1} in the lower excitonic level of the trimer (orange line in (a)) and at 16,000 cm^{-1} in the monomer (light blue line in (b)) are detected via two-dimensional electronic spectroscopy (2DES). The energy relaxation kinetics are fitted with the sum of a Gaussian and damped sine function mentioned in the main text. The fitting results (red lines in (a) and dark blue lines in (b)) comprising the Gaussian decay component and the oscillation component are superimposed on the original kinetics (top) and oscillatory residual curves (bottom) for each panel. The damped oscillation decay (τ_c) time constants indicated on the curves reveal the dephasing of coherence.[15] (c) Comparison of the integrated coherence spectra between the monomer (blue) and trimer (orange) from 2DES (top) and heterodyne-detected transient grating (HDTG, bottom) measurements. The background noise level of the 2DES(HDTG)-detected coherence spectrum was about 14% (20%) of the integrated FT spectrum maximum. (d) Coherence spectra of dynamical Stokes shift measured via 2DES (top) and broadband transient absorption (BBTA, bottom) with the same excitation spectrum. The background noise level of the 2DES(BBTA)-detected coherence spectrum was about 21% (4%) of the FT spectrum maximum. The gray lines indicate vibrational modes observed in both spectra: 200, 270, 465, 515, 660, 805, 880, 1240, 1380, 1580, and 1640 cm^{-1}. The orange-shaded area shows the near-resonant frequency region in the trimer. All spectra were normalized to the amplitude at 200 cm^{-1}. (a, b) Reproduced with permission from ref 15. Available under a CC-BY license. Copyright 2024 Ruidan Zhu et al.

from the acquired population decay kinetics. For the α-subunit and monomer, the quantum coherence originates from pure vibrations.

2.3.1. Longer Exciton-Vibrational Coherence Time Was Observed in the APC Trimer than the Vibrational One in the Monomer. In a 2DES experiment, vibrational wave packets in the excited state are generated by impulsive laser excitation. Subsequently, the excited state relaxes through intra- and intermolecular vibrational relaxation as well as solvent reorganization. This energy relaxation, known as the dynamic Stokes shift, is described by the Stokes shift function S(t). The oscillatory components of S(t) can be assigned to intramolecular vibrational modes, and Fourier transformation of S(t) gives rise to the coherence spectrum of dynamical Stokes shift. The dynamical Stokes shift S(t) can be well fitted with the sum of a Gaussian and damped sine function $f(t) = A_d \exp[-t^2/(2\tau_d^2)] + A_c \exp(-t/\tau_c)\sin(2\pi\omega \cdot t + \phi) + C$, where τ_d and τ_c are the decay and coherent lifetimes, respectively, A_d and A_c are the corresponding amplitudes, $\omega(\phi)$ is the oscillation frequency (phase), and C is the constant term. The energy relaxation dynamics, shown as the envelope with a decay lifetime (τ_d) of about 100 fs, were comparable for the trimer, monomer, and two subunits. This continuous relaxation of energy corresponds to the inertial solvation response of the protein and solvent.[83] However, we observed that the coherence vibrational lifetime (τ_c) was significantly shorter for the α-subunit (93 ± 19 fs) and the monomer (123 ± 30 fs) than for the exciton-vibrational trimer (501 ± 104 fs). These oscillations in S(t) originate from the coherent coupling of vibrational modes to electronic states as a wave packet.[84,85] Although a recent study also confirmed wave packet oscillations in S(t) for APC, it reported a shorter coherence time of about 200 fs.[86]

2.3.2. Half-Loss in Raman Intensities of the Resonant Modes Was Observed in the Coherent Spectra of APC. The coherence spectra were derived by projecting the 2D spectra along the excitation frequency, performing a Fourier transformation along the waiting time on the oscillatory residual and finally integrating the coherent amplitude along the emission frequency. For both the trimer and the α-subunit, 11 significant coherent frequencies were observed (gray lines in Figure 4c,d). Within the region that is near-resonant with the excitonic energy gap (orange-shaded area), two vibrational modes were assigned: ethylenic hydrogen out-of-plane (HOOP) wagging at 805 cm^{-1}, and a mixed mode involving HOOP bending, methine torsion, and ring rotation at 660 cm^{-1}. Interestingly, these asymmetric collective HOOP motions can modulate the inter-pigment distance. A comparison between the integrated coherent spectra of the trimer and the α-subunit (Figure 4c and Table 1 in ref 15) revealed a 49% ± 7% reduction in the amplitudes at the two near-resonant frequencies. No such amplitude reduction at the resonant frequencies was observed in the non-resonant Raman spectrum of the trimer with respect to that of the monomer (Supplementary Figure 8 in ref 15).

2.3.3. Absence of the Resonant Modes in the Dynamical Stokes Shift Was Observed in the Coherence Map. The dynamic Stokes shift coherence spectra from

https://doi.org/10.1021/acs.jpcb.5c07333
J. Phys. Chem. B 2026, 130, 4017−4040

2DES measurements were obtained by applying a Fourier transformation to the oscillatory residual curve of $S(t)$ at the lower excitonic level of the APC trimer and at the emission peak of the α-subunit (Figure 4d). These spectra show that the resonant modes almost completely disappeared in the APC trimer but not in the α-subunit. The fact indicates that these resonant modes do not participate in the energy dissipation of the lower excitonic level. Up until now, all the three predicted criteria for the quantum phase synchronization in the exciton vibration coupling for APC trimer have been verified experimentally.

2.4. Another Long-Lived Coherence in a Weak Coupling PE545 System

Cryptophyte is one of the most primitive photosynthetic organisms, surviving under relatively poor lighting conditions in the ocean and utilizing the sunlight more efficiently than terrestrial plants.[87] PE545 is the only type of phycobiliprotein in cryptophyte algae of the *Rhodomonas* and serves as their major light-harvesting antenna.[88,89] Recently, the coherence EET in PE545 has been investigated by 2DES[90,91] and theoretical modeling,[92−94] revealing quantum beating of at least 200 fs at room temperature. These observations provide compelling evidence for quantum coherent sharing of electronic excitation across the 5 nm-wide proteins under biologically relevant conditions.[91]

The structure of PE545 consists of four polypeptide chains, including two α-subunits (labeled as A and B) plus two β-subunits (labeled as C and D), arranged in a dimeric complex of $\alpha\beta$ monomers (Figure 1e, left panel). There are eight pigment molecules inside the PE545 dimer (Figure 1e, right panel), and all the pigments are covalently bound to the protein frame. A monomer contains three phycoerythrobilin (PEB 50/61, PEB 158, PEB 82) pigments in the β-subunit and one dihydrobiliverdin (DBV 19) pigment in the α-subunit. The closest pigments in the PE545 dimer, between PEB 50/61C and PEB 50/61D across the monomer−monomer interface, are separated by a center-to-center distance of 15 Å,[95] forming an excitonic dimer of the strongest coupling. The coupling constant has been estimated as 248 cm^{-1} by dipole−dipole approximation and 92 cm^{-1} by CIS/6-31G calculations.[95,96] The energy difference between the exciton levels of the PEB 50/61D-PEB 50/61C dimer is around 1080 cm^{-1}.

In contrast to the APC trimer, which contains three identical α84−β84 excitonic dimers, PE545 consists of only one relatively strongly coupled excitonic dimer (PEB 50/61C-PEB 50/61D) among its eight pigments, resulting in a congested absorption spectrum. The ultrafast EET process within the PEB 50/61 pigment pair with a lifetime constant of 50 fs for pure electronic dephasing was directly resolved. By monitoring the excited-state resolved dynamical Stokes shift in Figure 5, we observed a 270 fs exciton-vibrational coherence lifetime in the dimer, which is longer than the 120 fs vibrational coherence observed in the monomer. The shorter exciton-vibrational coherence time compared to that of the APC trimer is likely caused by the EET from the PEB 50/61 excitonic pair to lower energy pigments such as PEB 82C and DBVA.

Coherence spectra for the PE545 dimer and the monomer were derived from the corresponding 2DES. In the near resonance region, only one vibrational mode at 1150 cm^{-1} is observed, which is assigned to the C−C and C−N stretching coupled to N−H and C−H rocking.[97] Comparison of the

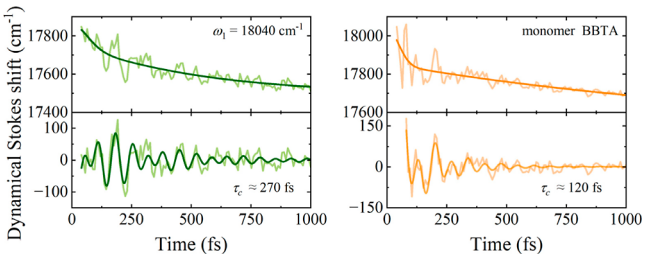

Figure 5. The 2DES-detected dynamical Stokes shift of PE545 dimer at ω_1 = 18,040 cm^{-1} (the lower excitonic level in the PEB 50/61D-PEB 50/61C pigment pair) and the BBTA-detected dynamical Stokes shift of the PE545 monomer. The energy relaxation kinetics are fitted with the sum of a Gaussian and single exponential decay function from 40 fs to 1 ps. The oscillatory residual curves plotted in the bottom panel, with the fitting results with the damped oscillation function from 40 to 1 ps for 2DES and from 80 fs to 1 ps for BBTA to avoid the jitter arising from the interference between the probe and the scattering light of pump.[19] Reprint with permission from ref 19. Copyright 2025 AIP Publishing.

dimer and monomer coherent spectra shows a negligible reduction in the amplitude for the 1150 cm^{-1} resonant mode. This can be attributed to two factors: first, the weak coupling in PE545 leads to only a minor reduction in the Raman intensity of the resonant mode; second, although PE545 contains six PEB and two DBV pigments, only two of PEBs form the electronic coupled pigment pair.

The excited-state resolved dynamical Stokes shift coherence spectra of the PE545 dimer and monomer, derived from the 2DES measurements, are shown in Figure 6a,c. These spectra reveal vibrational modes that participate in discrete excited-state energy levels. In the dimer, the near-resonant 1150 cm^{-1} mode is absent in the dynamical Stokes shift coherence spectrum detected at the lower excitonic level of the PEB50/61 excitonic dimer (Figure 6a, upper panel). However, this mode appears in the other energy levels of PEB 82C and DBV A in the dimer (Figure 6a, middle and lower panels) and is also present in the dynamical Stokes shift coherence spectrum of the PE545 monomer (Figure 6c). The resonant coupling of the 1150 cm^{-1} mode to the excitonic gap was further confirmed by the double-crossed heterodyne-transient grating (DC HD-TG) experiment. The polarization combination (45°, −45°, 90°, 0°) effectively distinguishes electronic and exciton-vibrational coherence from vibrational coherence by a significant suppression of the latter signal by a factor of ∼55 in the current case.[11,61,62] As shown in Figure 6d, in the all parallel polarization detection (AP HD-TG), the intensities of the 1150 cm^{-1} resonant mode are nearly identical for the PE545 dimer and monomer. In contrast, under DC HD-TG detection, the 1150 cm^{-1} mode is almost completely suppressed in the monomer (Figure 6e, lower panel), and it remains above the confidence of the noise level in the dimer (Figure 6e, upper panel).

The relative electronic coupling strength (also referred as the extent of exciton delocalization) is defined as $\left|\frac{V}{\Delta_s}\right| = \frac{2|J|}{\Delta_s}$, where $V = 2|J|$ is the excitonic coupling matric element and Δ_s is the difference between the site energies.[68,98] For the APC trimer, the relative electronic coupling strength is 0.42, and it is 0.17 for the PEB50/61 excitonic pair in PE545, taking J = 92 cm^{-1} and Δ_s = 1080 cm^{-1}. From Raman intensity loss for the coherent modes, the APC trimer belongs to the strong

https://doi.org/10.1021/acs.jpcb.5c07333
J. Phys. Chem. B 2026, 130, 4017−4040

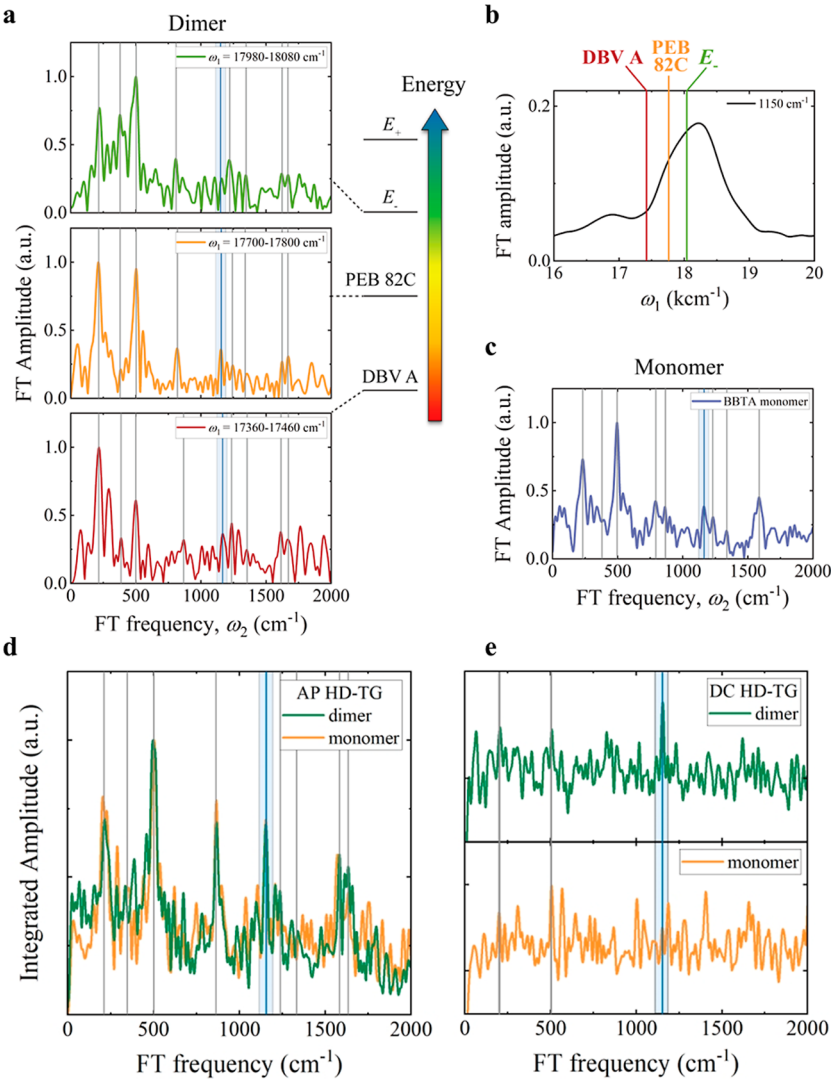

Figure 6. (a) Excited-state resolved dynamical Stokes shift coherence spectra from 40 fs to 1 ps of the PE545 dimer at ω_1 = 17,980−18,080 cm^{-1} (top), ω_1 = 17,700−17,800 cm^{-1} (middle), and ω_1 = 17,360−17,460 cm^{-1} (bottom), corresponding to the lower excitonic level of the PEB 50/61D-50/61C excitonic dimer, PEB 82C, and DBV A, respectively. The resonant mode at 1150 cm^{-1} is highlighted by a blue line, which is absent in the coherence spectrum at ω_1 = 17,980−18,080 cm^{-1} but appears in other spectra. (b) Intensity distribution of the 1150 cm^{-1} mode along excitation frequency ω_1 (integrated over the emission frequency ω_3) from pure absorptive 2DES of the PE545 dimer. (c) Dynamical Stokes shift coherence spectra from 80 fs to 1 ps of the PE545 monomer from BBTA measurements. (d, e) Comparison of the FT spectra of the PE545 dimer (green) and monomer (orange) from AP HD-TG (d) and DC HD-TG (e) measurements. The blue-shaded area highlights the mode at 1150 cm^{-1}.[19] (a−e) Reprint with permission from ref 19. Copyright 2025 AIP Publishing.

coupling case, while PE545 belongs to the weak coupling. Currently, this cannot be simply judged by the electronic coupling strength, since the modes in the excited state are vibronically excited, which are definitely related to their individual Huang-Phys factors.

2.5. Coherent versus Incoherent EET in PBS

The schematic structure of the PBS is shown in Figure 1a, with phycocyanin rods surrounding APC cores.[99,100] Two PC_{620} hexamers, a PC_{612} trimer, and various linker proteins compose a phycocyanin rod. PC_{620}, the outermost light-harvesting complex in the cyanobacterial PBS, is responsible for light collection and energy transfer to the core antenna APC. Downhill EET from the outer phycocyanin rods to the APC core has been observed in PBS by polarization-controlled 2DES, a technique that enhances the EET-related features[101] and 2DES signals.[102] The structure of the PC_{620} trimer and the spatial distribution of PCB pigments are shown in Figure 1c. Each monomer comprises three PCB pigments: α84 in the α-subunit and β155 and β84 in the β-subunit. α84 and β84 PCB are located on the inner areas, whereas β155 is located on the outer circumference of the protein. The closest chromophores in PC_{620} hexamer, between β84 and α84 from adjacent monomers, are separated by a center-to-center distance of only 21 Å.[103,104] The closest pigments in a single monomer, β84 and β155, are separated by 34 Å, while β155 and α84 are separated by 48 Å.[103,104] PC_{620} shares a nearly identical structure of the α84−β84 dimer with APC, including the comparable intermolecular distance (21 Å), the analogous angles between transition dipoles (55°),[99,100,105] and the same intermolecular coupling strength about 150 cm^{-1} obtained from fitting the spectral line width in APC and CPC from *Spirulina platensis*,[48] inferring an existence of possible coherent EET pathways. However, steady-state absorption and CD spectra show that there is no detectable excitonic splitting

https://doi.org/10.1021/acs.jpcb.5c07333
J. Phys. Chem. B 2026, 130, 4017−4040

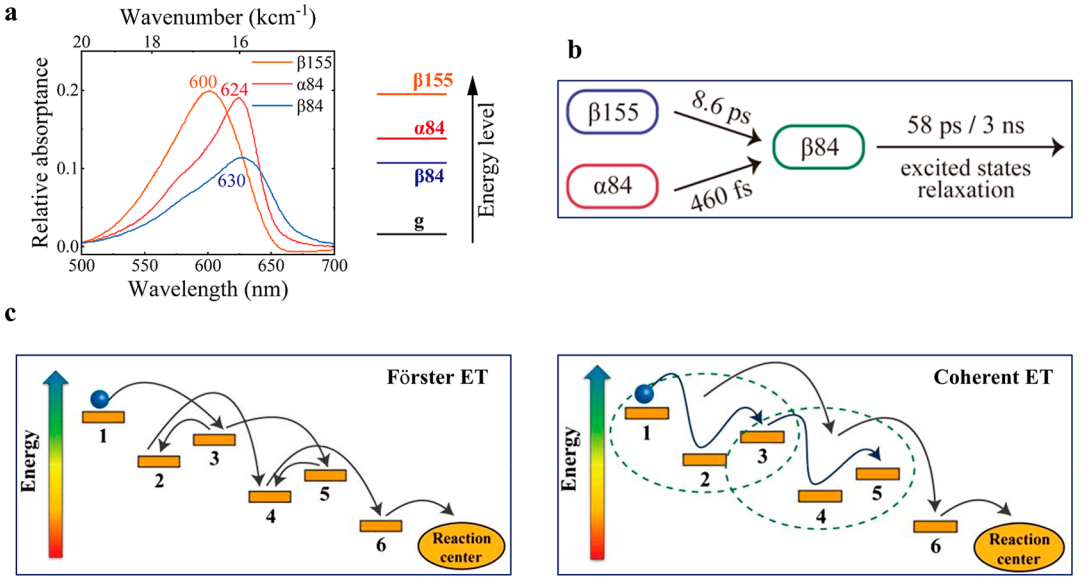

Figure 7. (a) Linear absorption spectra of β155 (orange), α84 (red), and β84 (blue) in monomeric phycocyanin at room temperature.[109] The energy level diagram of the three pigments is plotted on the right. (b) The EET model for global analysis.[14] (c) lustration sketching the difference between classical and quantum-coherent mechanisms of excitation energy transfer.[110,111] (a) Reprint with permission from ref 109. Copyright 1993 American Chemical Society. (b) Reprint with permission from ref 14. Copyright 2024 AIP Publishing. (c) Reprint with permission from ref 110. Copyright 2013 Royal Society of Chemistry.

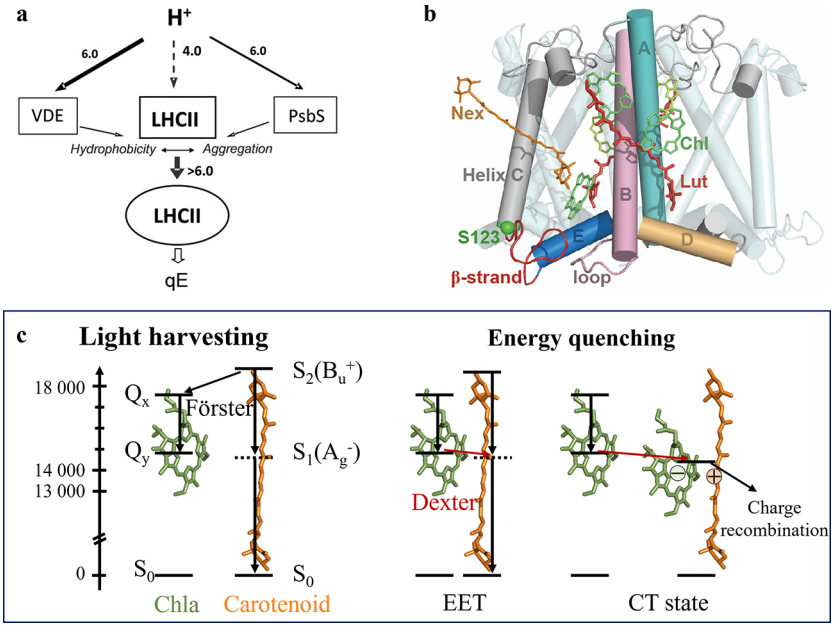

Figure 8. (a) Model explaining the effect of PsbS and the xanthophyll cycle on the pK_a of *q*E-active residues in LHCII in chloroplasts.[122] (b) The crystal structure of the LHCII trimer (PDB ID: 1RWT).[17] (c) Diagram of the NPQ mechanisms via EET and the CT state. (a) Reprint with permission from ref 121. Copyright 2012 Elsevier. (b) Reprint with permission from ref 17. Copyright 2020 Springer Nature.

between α84−β84 pigment pair in PC_{620}, and all the EET paths follow the FRET mechanism.[13] The EET in the PC_{620} was directly measured via polarization-controlled broadband 2DES at cross peaks by elimination of spectral broadening effects. The measured EET times are 460 fs from α84 to adjacent β84, 8.8 ps from β155 to β84, and 66.7 ps from β155 to α84 (Figure 7a,b).

The EET rates and their corresponding donor−acceptor distances well follow the FRET mechanism, i.e., $k_{FRET}(r) = \frac{1}{\tau_D}\left(\frac{R}{r}\right)^6$, where τ_D is the decay time of the donor in the absence of the acceptor, R is the Förster distance, and r is the distance between the donor and the acceptor.[106−108] Specifically, the EET from α84 to adjacent β84 follows a classical pathway with a time of 460 fs. This is notably slower than the corresponding transfer in the APC trimer (220 fs), which follows a coherent pathway, despite identical separation distance, orientation angle, and calculated coupling strength. Therefore, these results provide direct evidence that the coherent EET is faster, thus more efficient, than the incoherent transfer in the light-harvesting complexes (Figure 7c). We attributed the transition from coherent EET in the APC trimer

https://doi.org/10.1021/acs.jpcb.5c07333
J. Phys. Chem. B 2026, 130, 4017−4040

to incoherent EET in PC_{620} to the slight structural distortion of α84 PEB in PC_{620} with respect to its counterpart in APC, as shown in Figure 1d, lower panel), where the angle between pyrrole rings C and D is twisted from 3° in APC to 38° in PC_{620}. Other factors, such as pigment site energy differences induced by pigment−protein interaction, may also contribute.[48,102] Explicitly, as reported by Womick et al.,[48] the site energy gap for APC is 760 cm^{-1}, while for CPC, it is 350 cm^{-1}; therefore, the near resonant vibrational modes of 660 and 805 cm^{-1} for APC no longer hold for CPC (PC_{620}). It should be noted that coherent EET may provide alternative transfer pathways in the light-harvesting network, the energy transfer efficiency can be high in both coherent and incoherent EET regimes, and the biological advantage may lie in robustness or regulation, not the EET rate alone.

3. QUANTUM SWITCH REVERSIBLY REGULATING LIGHT HARVESTING AND PHOTOPROTECTION IN PHOTOSYNTHESIS OF HIGH PLANTS

3.1. Lut−Chl Pair as a Potential Nonphotochemical Quenching Site in LHCII

Under low-light conditions, most absorbed energy is transferred to the reaction center to drive photochemical reactions, while under high-light stress conditions, up to 80% of the absorbed energy is dissipated as heat to protect the reaction center from photodamage. This kind of thermal dissipation of excessive excitation energy is collectively termed as NPQ,[112−117] in which the dominant component is the pH-dependent energy quenching known as *q*E.[118] *q*E is mainly located within the LHCII (Figure 8a,b) and is triggered by the trans-membrane pH gradient. The formation and relaxation of NPQ are slower than those of the pH gradient, consequently, LHCII undergoes a reversible conformational transition during the NPQ formation and relaxation process.[119−121] Additionally, NPQ is potentially regulated by the xanthophyll cycle and the PsbS protein,[122] as shown in Figure 8a.[123,124] Historically, multiple quenching mechanisms have been proposed.[125] Currently, two principal models are supported by experiments and MD simulations. As shown in Figure 8c, the first involves EET from the excited Chl to the nearby carotenoid molecules and then quenched through heat dissipation,[126,127] which is mainly discussed in this featured article. Both in LHCII and CP29, the EET from Chla Q_y to the Car S_1 state has been detected.[127−130] The second involves charge transfer (CT) from Lut to Chl, forming a Chl^-−Lut^+ CT state, and the excited Chl is quenched by the Chl^-−Lut^+ CT state through charge recombination.[131−133] Nonetheless, the MD simulation and quantum chemical calculations show that the CT state quenching can be selective and to occur only in the L1 site, as the electronic coupling is sensitive to the Car−Chl distances and orientation and to different electric fields.[134]

The 2.72 Å crystal structure of LHCII (PDB ID: 1RWT)[135] reveals that LHCII is formed as a trimer. Each monomer consists of three transmembrane (TM) α-helices (A, B, and C), an amphipathic helix D, and a short 3_{10}-helix E (Figure 7b) on the luminal side of the thylakoid membrane. Each monomer binds eight Chl*a* molecules, six Chl*b* molecules, and four carotenoids. The carotenoid consists of two lutein molecules (Lut1 and Lut2), one neoxanthin (Nex), and one violaxanthin (Vio). Experiments also reveal that NPQ can be induced by elevated temperature both in vivo and in vitro.[136−138] In 2024, Ruan et al.[139] investigated the transient temperature rise of LHCII at the protein level, during which LHCII is heated by nonradiative dissipation of the excited pigments. With femtosecond and nanosecond time-resolved spectroscopy, approximately 7 °C temperature jump in the medium was observed at ∼60 ns after the laser excitation, and the conformational changes of LHCII in response to the transient raised temperature were also observed. These findings highlight the need for direct structural and mechanistic insight into the conformational transitions within LHCII. Specifically, how do protein dynamical structural changes regulate the switch between the light-harvesting and photoprotection states? The photoprotection state involves the efficient quenching of the excited state of Chl*a*, then what quantum principles does nature exploit to achieve this advantage?

The excited-state lifetime of Chl*a* in trimeric LHCII is shorter than that of free Chl*a* in solution (3.5 ns vs 5.5 ns).[140] Razi Naqvi hypothesized that this reduction could result from enhanced internal conversion due to interactions between Chl*s* and xanthophylls.[141,142] Later studies showed that in the photoprotective state, LHCII trimers and CP29 are sufficient for efficient EET from the excited state (Q_y) of Chls to the dark state (S_1) of Luts. Femtosecond transient absorption spectroscopy of LHCII in the dissipative state shows that energy is transferred from Chl*a* to a low-lying carotenoid excited state, identified as Lut1 in LHCII.[127] The electronic structure of xanthophyll is analogous to that of linear polyene with C_{2h} symmetry, and the ground state and the next two higher exited states are denoted as $S_0(1^1A_g^-)$, $S_1(2^1A_g^-)$, and $S_2(1^1B_u^+)$, respectively.[143] Based on the selection rule, the transition from S_0 to S_1 is forbidden, while the transition from S_0 to S_2 is allowed. The relative energy level of Lut and Chl*a* is presented in Figure 8c. It is expected that when the distance between Lut−Chl pair is larger than the van der Waals' contact distance, the energy would mainly transfer from the S_2 state of Lut to the excited state of Chl via FRET. Conversely, when the distance is close to or shorter than the van der Waals' contact distance, the excited-state energy in Chl*a* would be transferred to the S_1 (dark) state of Lut, which would be further dissipated as heat. Obviously, nature may use the distinct energy levels of the Lut−Chl pair as a quantum switch between the two states, i.e., light harvesting from Lut(S_2) to Chl*a* (Q_x) and energy quenching from Chl (Q_y) to Lut (S_1) states. A key remaining question, however, is how LHCII dynamically regulates the distance between Lut and Chl*a* in response to changes in light intensity.

3.2. Dynamical Structural Regulation Mechanism of NPQ in LHCII: A Scissoring Motion Model

Li et al.[144] investigated the dynamical and allosteric regulation mechanism of NPQ in LHCII using temperature-jump nanosecond time-resolved infrared (IR) spectroscopy (T-jump),[145] MD simulations, and quantum chemical computation. Through the time-resolved fluorescence spectra of LHCII at varied temperatures, acids, and extents of aggregation, it was found that both the increase in temperature and aggregation degree could lead to significant fluorescence quenching. Fluorescence lifetime analysis revealed three distinct states of LHCII: a light-harvesting state (H), an energy-quenching state (Q) with a shorter lifetime, and a denatured state (D) that appears at relatively high temperatures. T-jump and temperature-dependent Fourier transform infrared spectrometer (FTIR) measurements revealed that raising the temperature

https://doi.org/10.1021/acs.jpcb.5c07333
J. Phys. Chem. B 2026, 130, 4017−4040

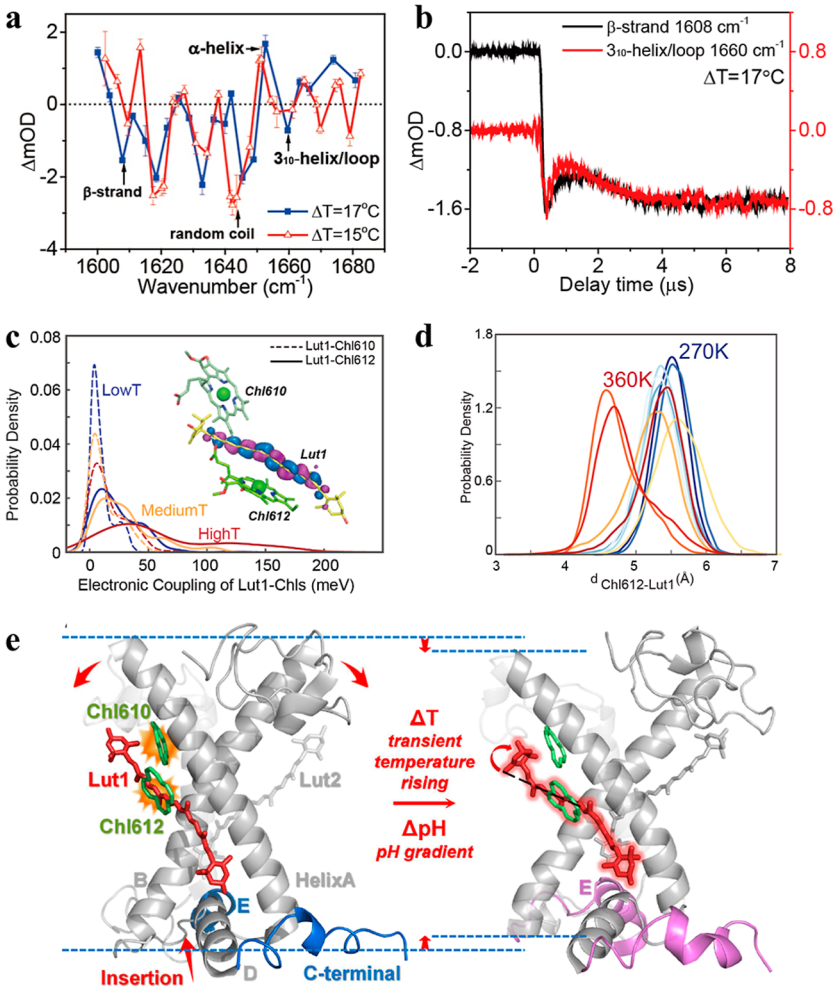

Figure 9. (a) Differential optical absorption (ΔOD) of IR spectra of LHCII trimers delayed by 8 μs. (b) Transient kinetics at 1608 and 1660 cm^{-1}; the overlap in bleaching kinetics indicates a cooperative conversion of 3_{10}-helix E/loop and antiparallel β-strands to α-helices. (c) Temperature-induced electronic couplings between Lut1 and Chl*a*. (d) Distribution of the Lut1−Chl612 distance at different temperatures. (e) Proposed dynamical allosteric regulation mechanism for light harvesting and photoprotection of LHCII trimers.[17] (a−e) Reprint with permission from ref 17. Copy 2020 Springer Nature.

(or decreasing the pH) induces a rapid conversion of the lumen side 3_{10}-helix E into a more compact α-helix (Figure 9a). The kinetics in Figure 9b indicates that the structural transition occurs with a time scale of 1 μs, after which the newly formed α-helix inserts into the hydrophobic core with a characteristic time constant of 1.24 μs.

The dynamic structural changes of LHCII at various temperatures and pH values were also investigated by all-atom MD simulations. The simulation results revealed that heating induces dehydration of specific protein subdomains at the luminal side, strengthening hydrophobic contacts. This, in turn, drives the conversion of 3_{10}-helix E and the C-terminal random coil of helix D into α-helices, and then the newly formed helical segments insert into the hydrophobic core. Such membrane-insertion motions of helices E and D generated an allosteric effect, pivoting scissoring motions of transmembrane (TM) helices A and B with R70−E180 and E65−R185 as salt bridges. As a result, the scissoring motion of TM helices drives the two associated Lut1 and Lut2 in a corresponding scissoring manner, thereby reducing the distances between lutein and its neighboring Chls. Furthermore, the electronic couplings and separation distance for Lut−Chl pigment pairs at various temperature were determined using MSDFT.[146] The results show that the electronic coupling between the dark S_1 state of Lut1 and the excited states of Chl610/Chl612 increases with temperature (Figure 9c), and the distribution of the Lut1−Chl612 distance shifts toward shorter distances as the temperature increases (Figure 9d). Moreover, the coupling of the Lut1−Chl612 pigment pair is markedly stronger than that of Lut1−Chl610, identifying Lut1−Chl612 as the principal energy quenching site in LHCII, consistent with a recent study reporting Lut1−Chl612 as a suitable NPQ candidate in CP29 under physiological conditions.[129] Based on transient spectroscopy measurements and MD simulations, a unified mechanism for the regulation of excess-energy dissipation in LHCII trimers under high temperature and low pH conditions (induced by intense sunlight) is proposed (Figure 9e). In this mechanism, the trimer operated as a molecular machine, and heat- and acidity-driven conversion of the 3_{10}-helix E and the C-terminal coil into a pair of α-helices generated forces that drive helices E and D toward the hydrophobic core within 1.24 μs. Two conserved salt−bridge pairs (R70−E180 and E65−R185) served as fulcrums, while luminal hydrophobic contacts between helices E−B and D−A acted as levers. Forces transmitted to the luminal ends of crossed TM helices A and B produced a pivot-scissoring motion of this TM helix pair.

https://doi.org/10.1021/acs.jpcb.5c07333
J. Phys. Chem. B 2026, 130, 4017−4040

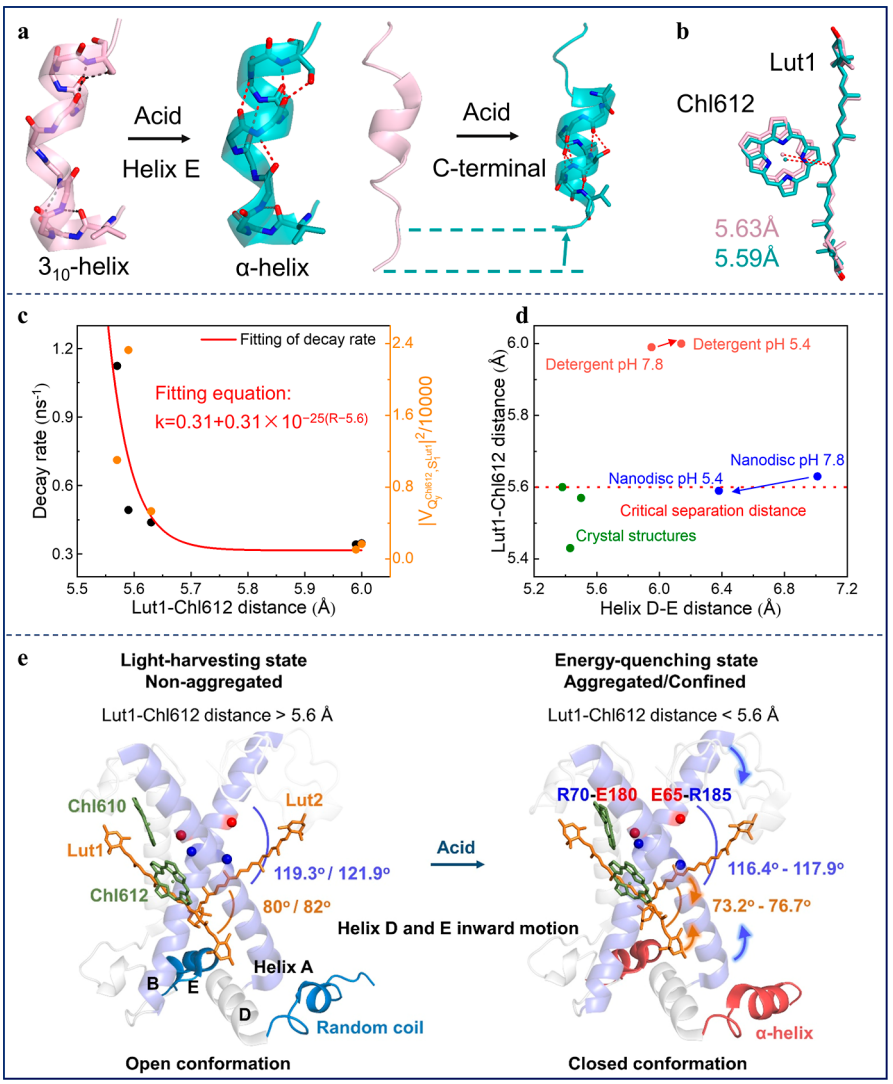

Figure 10. (a) Secondary structural comparison of helix E and the C-terminal in the LHCII nanodisc. (b) Comparison and distance of the Lut1−Chl612 pigment pair in the unprotonated and protonated structures of the LHCII nanodisc. (c) The relationship between the fluorescence decay rate (k = 1/fluorescence lifetime, black circles) and Lut1−Chl612 electronic coupling strength (orange circles) against the Lut1−Chl612 separation distance (R). (d) Plot of the helix D−E distance against the Lut1−Chl612 separation distance from different LHCII structures. (e) Structural model for the allosteric regulation mechanism and the key factors that drive state transition.[139] (a−e) Reprint with permission from ref 139. Copyright 2023 Springer Nature.

The resulting allosteric rearrangement shortened the distances between Lut and Chl pigments, most notably the Lut1−Chl612 pair, thereby markedly increasing their electronic coupling. Enhanced Lut1−Chl612 coupling provided an efficient quenching pathway for the Chl612 excited state, constituting the primary route for excess-energy dissipation.

3.3. LHCII Acting as a Quantum Switch Regulated by the Tuning of the Lut1−Chl612 Distance

In 2023, Ruan et al.[16] resolved six high-resolution cryo-EM structures of LHCII in detergent solution and LHCII confined in a nanodisc (LHCII-nanodisc) at pH 7.8 and 5.4. These six cryo-EM structures were identified as unprotonated and protonated structures based on their protonation states of D54 and E207 under different pH conditions. Upon protonation, remarkable secondary protein structural changes have been observed. Including a transition of 3_{10}-helix E into an α-helix and the formation of a new α-helix segment from the C-terminal random coil in helix D (Figure 10a), the corresponding density map of these local secondary structures can be found in Extended Data (Figure 6 in ref 139),[139] which are consistent with those from MD simulation.[17]

Although the protonation of LHCII either in detergent solution or in the nanodisc undergoes similar secondary structural changes, acid-induced fluorescence quenching has only been observed in the LHCII nanodisc. The fact suggests that lateral pressure (e.g., aggregation/confined in the nanodisc) is a prerequisite for LHCII to switch to the NPQ state, while acid-induced conformational changes enhance the fluorescence quenching, i.e., the protonated conformation is inequivalent to the quenching conformation. Analysis of the protein tertiary structural changes as those of helices D and E further shows that only for LHCII in the nanodisc that is subjected to lateral pressure, the changes in the secondary structure caused by the increased acidity can trigger the intercalation movement of helices D and E, which can result in a shorter Lut1−Chl612 distance (Figure 10d).

https://doi.org/10.1021/acs.jpcb.5c07333
J. Phys. Chem. B 2026, 130, 4017−4040

Protonation of LHCII induced a shear motion of TM helices A and B, indicated by the decreased helix A−B crossing angle (defined by the crossing angle between the Cα of T57-C69-R185-Q197), from 121.9° (unprotonated, pH 7.8) to 117.9° (protonated, pH 5.4) in the LHCII nanodisc and 119.3° to 116.6° in LHCII in detergent solution. A decreased helix A−B crossing angle brings a closer contact of the Lut1−Chl612 pair, while this distance does not change in response to the change in the helix A−B crossing angle for LHCII in detergent solution (5.99 Å vs. 6.00 Å). Furthermore, the Lut1−Chl612 distances were determined in varied cryo-EM structures, revealing that the Lut1−Chl612 distance is markedly shorter by about 0.4 Å in the LHCII nanodisc (5.63 Å and 5.59 Å at pH 7.8 and 5.4, Figure 10b) than that in detergent solution (5.99 Å and 6.00 Å at pH 7.8 and 5.4, respectively). These distances in the LHCII nanodisc were similar to those found in the crystal structure of significant fluorescence quenching (5.54 Å in 1RWT, 5.43 Å in 2BHW, and 5.60 Å in the cucumber crystal structure). Nonetheless, in all crystal and cryo-EM structures, the Lut1−Chl612 distance lies within a region of about 0.6 Å, while MD simulations reveal a far broader variability with Lut position or Lut1−Chl612 distance, which can fluctuate by 1 Å and even up to 2 Å.[134,144,147]

To quantitatively relate the fluorescence decay rates to the Lut1−Chl612 distances, the electronic coupling strength $V_{Q_y^{Chl612},S_1^{Lut1}}$ between the locally excited S_1 state of Lut1 and the Q_y state of Chl612 was calculated by MSDFT[146] for the varied cryo-EM structures and previously reported crystal structures. The calculated $V_{Q_y^{Chl612},S_1^{Lut1}}$, together with the corresponding experimentally measured fluorescence decay rates, is plotted as a function of the Lut1−Chl612 distance. The results show that the trends of the observed fluorescence decay rates and calculated electronic coupling constants are in remarkable agreement (Figure 10c). As the two pigments are in close spatial proximity, a Dexter model for EET was employed to fit both experimental and computational results,[148] that is, $k_{EET} = k_0 + k_{Chl612}^{Lut1} e^{-\beta(R-R_0)}$ (Figure 10c). The fit yields a critical distance value of 5.6 Å. When the Lut1−Chl612 distance exceeds 5.6 Å, Lut1 and Chl612 jointly capture light and transfer energy through the classical FRET through dipole−dipole interaction, and LHCII is in an efficient light-harvesting state. When the Lut1−Chl612 distance was shorter than 5.6 Å, the fluorescence of Chl612 could be mainly quenched through the Dexter energy transfer via electron exchange, since Chl612 is within the cluster of terminal emitters Chl610, 611, and 612.[149] A slight distance change around 5.6 Å is sufficient to enable LHCII to switch from the light-harvesting state to the energy-quenching state; thus, LHCII achieves reversible switching between Förster and Dexter energy transfer mechanisms through dynamical structure regulation. Though FRET can still contribute to excited energy quenching, its contribution becomes much smaller than that of Dexter energy transfer. Since Dexter energy transfer involves the spin exchange integral, it can be found that the Dexter exchange interaction scales with the product of orbital overlaps of donor−acceptor orbitals,[150] which enables Dexter energy transfer a feature of "quantum-ness". The structural data, combined with MD simulation results, directly confirm that Lut1−Chl612 is the main quenching site with a characteristic transition distance of 5.6 Å. Thus, Lut1−Chl612 pair acts as a quantum switch driven by the LHCII conformational change.

3.4. Accelerating the Quantum Switch as a Novel Strategy for Increasing the Photosynthetic Efficiency

In the natural environment, due to the leaf motions induced by the wind, the light environment of the plant canopy is constantly affected by fluctuating sunlight. Recovery from a photoprotective state to a light-harvesting state occurs on a time scale of minutes, whereas light intensity can change within seconds. This lag of recovery from photoprotection behind the sunlight intensity change results in a loss of photosynthetic efficiency. Zhu et al. examined this temporal mismatch in a dynamically illuminated canopy and found that when the rate of transition between photoprotective and light-harvesting states matched the instantaneous changes in solar irradiance, the CO_2 assimilation efficiency could increase by 17−32%.[151] It is known that NPQ is regulated by the xanthophyll cycle, acting jointly with photosystem II subunit S (PsbS).[152] The xanthophyll cycle functions as interconversion of Vio and zeaxanthin (Zea).[153] Vio is de-epoxidized by violaxanthin de-epoxidase (VDE) via the intermediate antheraxanthin (Ant) to generate Zea, which is then epoxidized back to Vio by zeaxanthin epoxidase (ZEP) under low light. PsbS and Zea speed up the formation of NPQ, whereas Vio promotes its relaxation back to the light-harvesting state.[154] In the absence of a complete understanding of the specific regulatory mechanisms at the molecular level, Long's group overexpressed PsbS, VDE, and ZEP, resulting in transgenic lines with faster transitions between the photoprotective and light-harvesting states.[155,156] Under natural outdoor illumination, these lines increased tobacco dry biomass by 15%[156] and soybean seed yield by 33%.[155] Thus, elucidating the quantum switch mechanism of NPQ at the molecular level may offer plant biologists a novel strategy to modulate NPQ through genetic engineering, with the ultimate goal of increasing crop productivity. Although this approach has been reported unsuccessful for some other species,[157,158] a comprehensive understanding of the NPQ mechanism remains essential.

4. MACROSCALE OPTIMAL SIZE OF ICM VESICLES REGULATED BY THE QUANTUM DESIGN PRINCIPLE IN THE LH2 STRUCTURE

In most purple bacteria, the photosynthetic system contains two types of antenna complexes: light-harvesting complexes 1 and 2 (LH1 and LH2). LH1 is known as the core complex surrounding the RC, whereas LH2 is the peripheral complex which transfers energy to LH1 and finally to RC for charge separation.[159−161] LH2 consists of 7−10 pairs of αβ-heterodimer subunits, each binding three bacteriochlorophyll a (BChl *a*) molecules and one carotenoid molecule.[162] Taking the structure of LH2 from the purple bacteria *Rps. acidophila* as an example (Figure 11),[163,164] the structure exhibits a high degree of symmetry with a 9-fold rotational axis defined by nine αβ-dipeptides. As shown in Figure 11, the total 27 BChl *a* form two concentric rings. One with 9 BChl *a* of a larger inter-pigment separation is known as the B800 ring (with light absorption maximum at 800 nm), and another with 18 BChl *a* of shorter inter-pigment separation is known as the B850 ring (with light absorption maximum at 850 nm). The B850 ring acts as both an energy collector and storage, preserving excitation energy until it is forwarded to other rings and ultimately to the RCs, with an overall quantum efficiency as high as 95%.[165] Different spectroscopic studies of LH2[166−168] revealed that, unlike those in the crystal form, the isolated LH2

https://doi.org/10.1021/acs.jpcb.5c07333
J. Phys. Chem. B 2026, 130, 4017−4040

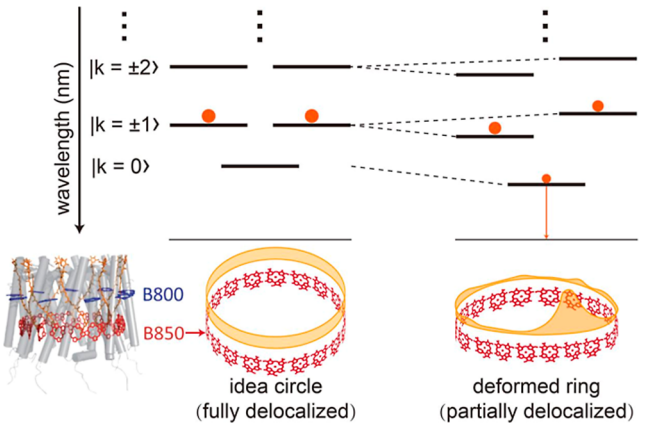

Figure 11. Schematic diagrams illustrating the LH2 crystal structure and excitonic energy levels and exciton delocalization of the B850 pigment ring. The filled orange circles represent the population distribution of a given excited state. The red Bchl *a* ring symbolizes the B850 ring, while the yellow band signifies the extent of exciton delocalization across the B850 ring.[98,173] In the case of a perfectly symmetric B850 ring, the excitation energy is initially delocalized across all 18 BChl *a* molecules. Any departure from this situation results in energy level splitting of the degenerated states and the localization of excitation energy on a few BChl *a* molecules. The lowest excitonic state becomes partially optical-transition allowed.[18,178] Reprint with permissin from ref 18 and 178. Available under a CC-BY license. Copyright 2025 Ying Zhang et al. Copyright 2018 Royal Society of Chemistry.

molecule deforms from a ring of C_9 symmetry to an elliptical shape of C_2 symmetry. Hong et al. observed the topological structure of LH2 from *Rb. sphaeroides* 2.4.1 in detergent solutions by small-angle X-ray scattering (SAXS). LH2 adopted an elliptical shape with an eccentricity of 0.59.[169] It has been shown that the ring structure of B850 possesses unique properties for solar energy storage and transfer, enabling delocalization of an exciton on the Bchl *a* ring. It is generally agreed that these excitonic states are not completely delocalized. After the initial interlevel excitonic relaxation,[170] the excitonic states would be trapped at a delocalization length of 4−6 molecules.[171,172] According to the excitonic theory, which disregards site energy disorder and protein structure deformation, the upper pair of degenerated excitonic energy levels ($k = \pm 1$) are optically allowed, whereas the lowest excited state ($k = 0$) is optically forbidden (Figure 11). Once excitation relaxes into this forbidden state, it is preserved, enabling the B850 ring to act as both an energy storage and an efficient energy donor; this is a functional consequence of quantum design principles. Once the 9 fold symmetry is broken to a C_2 symmetry (elliptical deformation), the lowest excited state becomes partially optically allowed.[173] More recent theoretical work shows that splitting of energy levels which makes $k = 0$ state super-radiant may not involve LH2 elliptical distortion, correlated site energy disorders, or mixing of the B850 exciton and CT states and can also lead to the realization of splitting of the B850 degenerated states.[174−176] Chen et al. also showed that when LH2 is adsorbed on SiO_2 nanoparticles, its excited-state lifetime decreases. In this case, a larger site energy disorder is introduced, which is correlated to the curvature of the nanosphere. Later, LH2 adsorbed on SiO_2 nanoparticles has been experimentally confirmed by silica shell-isolated Au nanoparticle-enhanced Raman spectroscopy.[177] Therefore, it is expected that any structural distortions of LH2 deviating from the plane of the pigment ring would lead to exciton energy splitting, accompanied by additional fluorescence radiation loss and shortened excited state lifetimes, thereby reducing the EET efficiency.

Experimental observations show that under low-light conditions, the ICM of photosynthetic bacteria invaginates to form numerous vesicles to increase the light-harvesting area. However, the curved surfaces of these vesicles may distort LH2, giving rise to a reduction in the EET efficiency. Explicitly, when the lifetime of B850 at room temperature is about 1.3 ns and the trapping time is about 100 ps,[42] the EET efficiency (η) is around 93%. If the lifetime of LH2 is reduced to 0.7 ns, then η drops to about 87%. Therefore, photosynthetic bacteria must strike an optimal balance between "increasing light-harvesting area by increasing the number of vesicles of smaller size" and "maintaining efficient EET with a larger vesicle size for less distorted LH2" through vesicle size optimization. It has been observed that the vesicle size has an optimal distribution around the 50−80 nm range. The optimal design of nanoscale LH2 structures has been explored in relation to quantum effects.[162] At a larger spatial scale, a kinetic model has suggested that the formation of ICM vesicles in response to light adaptation of bacteria is a spontaneous optimization process balancing structural integrity and robust energy conversion.[179] Our study further revealed that quantum design principles governing the B850 electronic state also regulate the optimal size of photosynthetic vesicles. To elucidate this optimization strategy, we used negatively charged silica nanoparticles with sizes ranging from 15 to 550 nm to simulate curvature-induced LH2 deformation on the vesicles,[18] since preparation of artificial vesicles (liposomes) with systematic variation of the size in a range from tens of nanometers to sub-micrometers is currently infeasible.

4.1. Quantitative Description of LH2 on Silica Nanoparticles

Du et al. showed that LH2 adheres to the silica nanoparticle surface, with the positively charged cytoplasmic side (N-terminal) of LH2 oriented toward the negatively charged nanoparticle surface.[177] Subsequently, Shi et al. determined the surface charge density of silica nanoparticles (SiO_2) of varying sizes in solution, revealing that the surface charge density is approximately proportional to the curvature of the nanoparticle, $\rho \propto 1/d$, where ρ is the surface density and d is the diameter of SiO_2.[180] When the elastic LH2 plate interacts with a charged spherical nanoparticle, the Coulombic interaction between them induces two distinct types of deformation: in-plane elliptical deformation and out-of-plane bending deformation. It is shown that when d is larger than 13.7 nm, the LH2 would assume a ring form rather than an ellipse. Thus, only the out-of-plane deflection is considered. When d is larger enough, considering the softness of the LH2 plate, it is expected that LH2 would self-adapt to the curvature of the nanosphere, and the relation between the vertical deflection Δz and d can be approximated as

$$\Delta z \approx \frac{r_0^2}{2d} \propto \frac{1}{d} \tag{3.1}$$

where r_0 is the radius of the LH2 ring.

As the nanoparticle size decreases, the bending stiffness of LH2 hinders its yield to match the curvature of the nanoparticles. An elastic plate deflection model is employed where the central part of the LH2 plate is supported by a

https://doi.org/10.1021/acs.jpcb.5c07333
J. Phys. Chem. B 2026, 130, 4017−4040

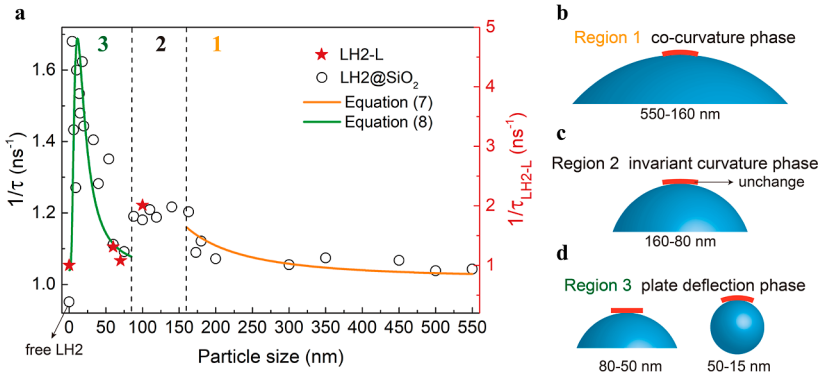

Figure 12. The measured B850 excited-state decay rate $(1/\tau)$ against the silica particle (or liposome) size and theoretical fitting. (a) The excited-state lifetime was measured by femtosecond time-resolved transient absorption of LH2@SiO_2, together with LH2 in liposomes with varying sizes. The curves for the size-dependent decay rate for LH2@SiO_2 against the nanoparticle size can be divided into three regions: (b) the co-curvature phase in region 1 for larger particle size; (c) the invariant LH2 curvature phase in region 2 resulting from the bending stiffness of the LH2 plate; and (d) the plate deflection phase in region 3 for small particle sizes.[18] Reprint with permission from ref 18. Available under a CC-BY license. Copyright 2025 Ying Zhang et al.

fulcrum, while the edge of the plate experiences an applied shear force from the vertical Coulombic force component. Consequently, the deflection w of an isotropic elastic plate satisfies the Lagrange equation

$$D\nabla^4 w = 0 \tag{3.2}$$

where D is the flexural rigidity of the plate.[181] By solving differential eq 3.2, vertical deformation for small particle sizes is derived as

$$\Delta z = w_{\max} \propto \rho/(1 + 4r_0^2/d^2)^{3/2} \approx 1/d(1 + 4r_0^2/d^2)^{3/2} \tag{3.3}$$

where ρ is the surface charge density of the silica nanoparticle, and $w_{\max}$ is the maximum deflection of the LH2 plate at its edge.

4.2. Correlation between the Excited-State Lifetime of B850 and LH2 Deflection

The Hamiltonian for B850 is[166,182]

$$\mathrm{H} = \sum_{n=1}^{18} E_n |n\rangle\langle n| + \sum_{n=1}^{18}\sum_{m=1}^{2} \mathrm{t}_{n,n+m}[|n\rangle\langle n+m| + |n+m\rangle\langle n|] \tag{3.4}$$

where E_n represents the site energy of the nth individual BChl a molecule, and $\mathrm{t}_{n,n+1}$ and $\mathrm{t}_{n,n+2}$ are the nearest and second-nearest neighboring interaction, respectively. The local excited states are denoted by $|n\rangle$ and $|n+m\rangle$, where $m = 1$ or 2. The coherent one-exciton eigenfunction of the Hamiltonian[183] is expressed as $|k\rangle = \sum_{n=1}^{18} c_{kn}|n\rangle$, with corresponding coefficients c_{kn}. The dipole oscillator strength (f_k) of the excitonic state $|k\rangle$ is given by $f_k = \vec{\mu}_k^* \cdot \vec{\mu}_k$, where $\vec{\mu}_k$ is obtained from $\sum_{n=1}^{18} c_{kn}\vec{\mu}_n$, and $\vec{\mu}_n$ represents the transition dipole moment for the Q_y band of nth BChl a.[184,185] To describe the spherical deformation, the atomic coordinates of planar LH2 were mapped onto spherical patches by using a length-preserving transformation. The oscillator strengths of the lowest excitonic state were calculated at varying bending deflections. The results reveal that the oscillator strength of bent LH2 can be fitted by

$$f \propto \Delta z^2 \tag{3.5}$$

Since $f \propto k_r$, where k_r is the radiative decay rate, if k_r is determined, then deformation-induced lifetime shorting of LH2 can be verified experimentally. The excited-state decay lifetime τ includes contributions from both the radiative decay rate (k_r) and nonradiative decay rate (k_{nr}). Generally, with the known fluorescence quantum yield $(\phi = k_r/(k_r + k_{nr}) = k_r\tau)$, k_r can be determined from the measured τ. However, due to a significant scattering effect from the SiO_2 particles of large sizes, ϕ cannot be determined accurately. Zhang et al. showed that there exists a proportional relationship between radiative and nonradiative rates given by $k_{nr}(T) \approx (k_{nr}^0/k_r^0)k_r(T) + [A(T) - B(T)]k_{nr}^0$, where k_{nr}^0 and k_r^0 are the rate constants at $T = 0$ K, while $A(T)$ and $B(T)$ are experimentally determined coefficients at temperature T,[186] and they further showed that this linear relationship also holds true for LH2@SiO_2 with varied particle sizes. Combining eqs 3.1, 3.3, and 3.5, the relations between the inverse excited-state lifetime and the nanoparticle diameter are obtained as

$$1/\tau \propto 1/d^2 \tag{3.6}$$

for large particle size, and

$$1/\tau \propto 1/[d^2(1 + 4r_0^2/d^2)^3] \tag{3.7}$$

for small particle size.

4.3. Deformation-Induced B850 Lifetime Changes: Comparison between Theoretical and Experimental Results

Figure 12 demonstrates the measured B850 excited-state decay rate of LH2@SiO_2 from *Rba. sphaeroides* against the size of the nanoparticles. Three distinct deformation regions are observed, as represented in Figure 12a. Region 1 (550 → 160 nm): in this larger size region, the bending deformation of LH2 aligns well with eq 3.6 of co-curvature deformation represented by the orange solid curve. Region 2 (160 → 80 nm): the lifetime remains relatively constant, which has not been predicted in theory. The fact suggests that the deformation remains unchanged due to the bending stiffness of the LH2 plate; it also implies an intrinsic curvature diameter of approximately 160 nm for LH2, consistent with the previous MD simulations result.[187] Region 3 (15 → 80 nm): as the particle size further decreases to around 80 nm, a sudden decrease appears, indicating a significant alleviation in LH2 deformation. This

https://doi.org/10.1021/acs.jpcb.5c07333
J. Phys. Chem. B 2026, 130, 4017−4040

abrupt change suggests that the LH2 plate almost returns to its near-flat structure due to the increased separation distance between the nanoparticle surface and the LH2 plate's edge. The electrostatic attraction becomes insufficient to dominate over the resilience of LH2, causing LH2 to revert to a near-flat form. The experimental data in this region can be fitted with eq 3.7. To support the rationality of using silica nanospheres instead of vesicles, the lifetimes of the B850 of LH2 embedded in liposomes of several typical averaged sizes (60, 70, 100 nm) are also plotted in Figure 12 (red pentagrams). Apparently, the observed curvature-induced changes in LH2 lifetime in liposomes exhibit a consistent trend with those observed for LH2@SiO_2 of similar sizes. This consistency reinforces the experimental approach of substituting liposomes with silica nanoparticles.

This study reveals that optimizing the photosynthetic vesicle size requires LH2 to maintain quantum-optimized electronic states. It demonstrates how 10 nm-scale quantum design principles regulate larger organelles, extending "quantum biology" research from molecular to organelle levels, giving an example for macroscopic quantum effects, i.e., from sub 10 nm-scale LH2 quantum design to a scale of 50−80 nm in optimized photosynthetic vesicles and possibly to the whole cell in a micrometer scale to achieve high photosynthetic efficiency.

5. CONCLUSIONS AND OUTLOOK

In this featured article, we demonstrate that nature exploits quantum effects in photosynthesis across a wide range of spatial and temporal scales. The key findings are summarized as follows:

- The correlation between the spatial delocalization and the excited-state lifetime of pigments is fundamental to harnessing quantum effects for biological advantages. Specifically, LHCII regulates the state transition between light harvesting and photoprotective states with a critical Lut1−Chl612 distance of 5.6 Å, tuning the LHCII excited-state lifetime from approximately ∼4 ns to ∼200 ps.[188,189] In APC, the delocalization of excitation energy across the α84−β84 PCB pair at a distance of up to 21 Å results in a transition from an incoherent EET time of 460 fs (PC_{620}) to a coherent EET time of 220 fs. In photosynthetic bacteria, the macroscale optimal size of ICM vesicles preserves the typical quantum design features of the LH2 structure at a diameter of 50−80 nm, with an excited-state B850 lifetime ranging from about 700 ps for curved LH2 to 1 ns for flat LH2.
- Proteins act as active regulatory partners, not merely passive scaffolds. In all these cases, proteins are not just frameworks to bind pigments but are vital components in the realization of quantum effects. For instance, APC maintains the precise configuration of its PCB pigments, LHCII regulates its compactness (aggregation state) and secondary structure in response to heat and pH changes to trigger the quantum switch, and LH2 ensures the robustness to maintain the rigidity of the plane structures. Consequently, it is the combined contribution of both pigments and their associated protein structures that results in the observed quantum effects.
- Quantum phase synchronization in excitonic dimers could be a general mechanism for coherent EET. It is an active mechanism that protects exciton-vibrational coherence against environmental fluctuations by sacrificing nearly 50% of the energy from the resonant vibrational modes (energy-dissipating antisymmetric collective modes).

Further manifestations of biological quantum effects are anticipated in photosynthetic systems, from individual light-harvesting complexes and reaction centers to their larger assemblies, complete photosystems, and even entire cells, as well as in artificial photosynthetic architectures. Moreover, the principle of noise-resilient quantum phase synchronization may be applied to other fields requiring long coherence times, such as quantum computations.[190]

AUTHOR INFORMATION

Corresponding Author

Yuxiang Weng − *Beijing National Laboratory for Condensed Matter Physics, Institute of Physics, Chinese Academy of Sciences, Beijing 100190, China; University of Chinese Academy of Sciences, Beijing 100049, China; Songshan Lake Materials Laboratory, Dongguan 523808 Guangdong, China;* orcid.org/0000-0003-0423-2266; Email: yxweng@iphy.ac.cn

Author

Meixia Ruan − *Beijing National Laboratory for Condensed Matter Physics, Institute of Physics, Chinese Academy of Sciences, Beijing 100190, China*

Complete contact information is available at: https://pubs.acs.org/10.1021/acs.jpcb.5c07333

Notes

The authors declare no competing financial interest.

Biographies

Meixia Ruan received her Bachelor's degree in 2018 from Sichuan University. In 2024, she received a Ph.D. degree in optics from the Institute of Physics, CAS. Her research is centered on the dynamical regulation mechanism of light-harvesting complexes to switch between varied states, using the time-resolved spectroscopic and cryo-EM studies.

https://doi.org/10.1021/acs.jpcb.5c07333
J. Phys. Chem. B 2026, 130, 4017−4040

Yuxiang Weng, a Professor in the Institute of Physics in China, received his Bachelor's and Master's degrees from the Department of Chemistry at East China Normal University in 1985 and 1988, respectively. In 1993, he earned his Ph.D. in optics from the Institute of Physics (IOP), CAS. He conducted postdoctoral research from 1994 to 1999 at the University of Hong Kong and Emory University in the United States. He has been working in IOP since 1999 and was supported by National Science Foundation for Distinguished Young Scholars of China in 2009. Currently, Professor Weng's research focuses on the time-resolved spectroscopic study of coherent energy transfer in photosynthetic systems (quantum biology in photosynthesis), photogenerated carriers in artificial photosynthetic systems, and the protein dynamic structure in regulation of its function. He has led the development of femtosecond TAS, femtosecond fluorescence noncollinear optical parametric amplification spectroscopy, femtosecond two-dimensional electron spectroscopy, and a number of other time-resolved spectroscopic equipment.

■ ACKNOWLEDGMENTS

This work was supported by the Natural Science Foundation of China (T2350011). We thank Jiading Zou and Hanting Meng for their help in preparing the revised manuscript.

■ REFERENCES

(1) Mirkovic, T.; Ostroumov, E. E.; Anna, J. M.; van Grondelle, R.; Govindjee; Scholes, G. D. Light Absorption and Energy Transfer in the Antenna Complexes of Photosynthetic Organisms. *Chem. Rev.* **2017**, *117* (2), 249−293.

(2) Blankenship, R. E. *Molecular mechanisms of photosynthesis*; Blackwell Science, 2002.

(3) Song, Y.; Qin, C.; Dong, S.; Li, X.; Wei, A.; Zhang, G.; Chen, R.; Hu, J.; Zeng, G.; Xiao, L.; Jia, S. Quantum Coherence Effect in the Interaction of Light and Molecules. *Laser Photonics Rev.* **2024**, *18* (6), 2400093.

(4) Romero, E.; Novoderezhkin, V. I.; van Grondelle, R. Quantum design of photosynthesis for bio-inspired solar-energy conversion. *Nature* **2017**, *543* (7645), 355−365.

(5) van Grondelle, R.; Novoderezhkin, V. I. In Quantum effects in photosynthesis, *22nd Solvay Conference on in Chemistry*, 2011, pp 198−210.

(6) Brookes, J. C. Quantum effects in biology: golden rule in enzymes, olfaction, photosynthesis and magnetodetection. *Proc. R. Soc. A:Math. Phys. Eng. Sci.* **2017**, *473* (2201), 20160822.

(7) Fleming, G. R.; Scholes, G. D.; Cheng, Y.-C. In *Quantum effects in biology*. *22nd Solvay Conference on Chemistry*, 2011, pp 38−57.

(8) Duan, H.-G.; Jha, A.; Chen, L.; Tiwari, V.; Cogdell, R. J.; Ashraf, K.; Prokhorenko, V. I.; Thorwart, M.; Miller, R. J. D. Quantum coherent energy transport in the Fenna-Matthews-Olson complex at low temperature. *Proc. Natl. Acad. Sci. U. S. A.* **2022**, *119* (49), No. e2212630119.

(9) Kong, F.-F.; Tian, X.-J.; Zhang, Y.; Zhang, Y.; Chen, G.; Yu, Y.-J.; Jing, S.-H.; Gao, H.-Y.; Luo, Y.; Yang, J.-L.; Dong, Z.-C.; Hou, J. G. Wavelike electronic energy transfer in donor-acceptor molecular systems through quantum coherence. *Nat. Nanotechnol.* **2022**, *17* (7), 729−736.

(10) Cao, J.; Cogdell, R. J.; Coker, D. F.; Duan, H.-G.; Hauer, J.; Kleinekathöfer, U.; Jansen, T. L. C.; Mancal, T.; Miller, R. J. D.; Ogilvie, J. P.; Prokhorenko, V. I.; Renger, T.; Tan, H.-S.; Tempelaar, R.; Thorwart, M.; Thyrhaug, E.; Westenhoff, S.; Zigmantas, D. Quantum biology revisited. *Sci. Adv.* **2020**, *6* (14), No. eaaz4888.

(11) Thyrhaug, E.; Tempelaar, R.; Alcocer, M. J. P.; Zidek, K.; Bina, D.; Knoester, J.; Jansen, T. L. C.; Zigmantas, D. Identification and characterization of diverse coherences in the Fenna-Matthews-Olson complex. *Nat. Chem.* **2018**, *10* (7), 780−786.

(12) Nalbach, P.; Braun, D.; Thorwart, M. Exciton dynamics and Quantumness of energy transfer in the Fenna-Matthews-Olson complex. *Phys. Rev. E Stat Nonlin Soft Matter Phys.* **2011**, *84* (4), 983−988.

(13) Ball, P. Is photosynthesis quantum-ish? *Phys. World* **2018**, *31* (4), 44−48.

(14) Wang, J.; Zhu, R.; Zou, J.; Liu, H.; Meng, H.; Zhen, Z.; Li, W.; Wang, Z.; Chen, H.; Pu, Y.; Weng, Y. Incoherent ultrafast energy transfer in phycocyanin 620 from Thermosynechococcus vulcanus revealed by polarization-controlled two dimensional electronic spectroscopy. *J. Chem. Phys.* **2024**, *161* (8), 085101.

(15) Zhu, R.; Li, W.; Zhen, Z.; Zou, J.; Liao, G.; Wang, J.; Wang, Z.; Chen, H.; Qin, S.; Weng, Y. Quantum phase synchronization via exciton-vibrational energy dissipation sustains long-lived coherence in photosynthetic antennas. *Nat. Commun.* **2024**, *15* (1), 3171.

(16) Ruan, M.; Li, H.; Zhang, Y.; Zhao, R.; Zhang, J.; Wang, Y.; Gao, J.; Wang, Z.; Wang, Y.; Sun, D.; Ding, W.; Weng, Y. Cryo-EM structures of LHCII in photo-active and photo-protecting states reveal allosteric regulation of light harvesting and excess energy dissipation. *Nat. Plants* **2023**, *9* (9), 1547−1557.

(17) Li, H.; Wang, Y.; Ye, M.; Li, S.; Li, D.; Ren, H.; Wang, M.; Du, L.; Li, H.; Veglia, G.; Gao, J.; Weng, Y. Dynamical and allosteric regulation of photoprotection in light harvesting complex II. *Sci. China:Chem.* **2020**, *63* (8), 1121−1133.

(18) Zhang, Y.; Chu, Q.; Du, L.; Yao, Y.; Chen, H.; Wang, P.; Zhang, J.; Chen, M.; Peng, L.; Weng, Y. Macroscale optimal size of ICM vesicles regulated by quantum design principle in LH2 structure. *Biophys. J.* **2025**, *124* (14), 2317−2326.

(19) Wang, J.; Zou, J.; Zhen, Z.; Meng, H.; Liao, G.; Liu, L.; Wang, Z.; Chen, H.; Pu, Y.; Weng, Y. Quantum phase synchronization revealing few-hundred femtosecond coherence in cryptophyte phycoerythrin 545 antenna from exciton-vibrational coupling. *J. Chem. Phys.* **2025**, *162* (20), 205101.

(20) Romero, E.; Augulis, R.; Novoderezhkin, V. I.; Ferretti, M.; Thieme, J.; Zigmantas, D.; Van Grondelle, R. Quantum coherence in photosynthesis for effcient solar-energy conversion. *Nat. Phys.* **2014**, *10* (9), 677−683.

(21) Panitchayangkoon, G.; Hayes, D.; Fransted, K. A.; Caram, J. R.; Harel, E.; Wen, J. Z.; Blankenship, R. E.; Engel, G. S. Long-lived quantum coherence in photosynthetic complexes at physiological temperature. *Proc. Natl. Acad. Sci. U. S. A.* **2010**, *107* (29), 12766−12770.

(22) Collini, E.; Wong, C. Y.; Wilk, K. E.; Curmi, P. M. G.; Brumer, P.; Scholes, G. D. Coherently wired light-harvesting in photosynthetic marine algae at ambient temperature. *Nature* **2010**, *463* (7281), 644−647.

(23) Engel, G. S.; Calhoun, T. R.; Read, E. L.; Ahn, T. K.; Mančal, T.; Cheng, Y. C.; Blankenship, R. E.; Fleming, G. R. Evidence for wavelike energy transfer through quantum coherence in photosynthetic systems. *Nature* **2007**, *446* (7137), 782−786.

(24) Jha, A.; Zheng, F.; Liu, Z.; Mukamel, S.; Thorwart, M.; Miller, R. J. D.; Duan, H.-G. Quantum coherent dynamics in photosynthetic protein complexes. *Chem. Soc. Rev.* **2025**, *55*, 1089−1130.

(25) Lorenzoni, N.; Lacroix, T.; Lim, J.; Tamascelli, D.; Huelga, S. F.; Plenio, M. B. Full microscopic simulations uncover persistent

https://doi.org/10.1021/acs.jpcb.5c07333
J. Phys. Chem. B 2026, 130, 4017−4040

quantum effects in primary photosynthesis. *Sci. Adv.* **2025**, *11* (40), No. eady6751.
(26) Jumper, C. C.; van Stokkum, I. H. M.; Mirkovic, T.; Scholes, G. D. Vibronic Wavepackets and Energy Transfer in Cryptophyte Light-Harvesting Complexes. *J. Phys. Chem. B* **2018**, *122* (24), 6328−6340.
(27) Jumper, C. C.; Rafiq, S.; Wang, S.; Scholes, G. D. From coherent to vibronic light harvesting in photosynthesis. *Curr. Opin. Chem. Biol.* **2018**, *47*, 39−46.
(28) Ramanan, C.; Ferretti, M.; van Roon, H.; Novoderezhkin, V. I.; van Grondelle, R. Evidence for coherent mixing of excited and charge-transfer states in the major plant light-harvesting antenna, LHCII. *Phys. Chem. Chem. Phys.* **2017**, *19* (34), 22877−22886.
(29) Novoderezhkin, V. I.; Romero, E.; Prior, J.; van Grondelle, R. Exciton-vibrational resonance and dynamics of charge separation in the photosystem II reaction center. *Phys. Chem. Chem. Phys.* **2017**, *19* (7), 5195−5208.
(30) Scholes, G. D.; Fleming, G. R.; Chen, L. X.; Aspuru-Guzik, A.; Buchleitner, A.; Coker, D. F.; Engel, G. S.; van Grondelle, R.; Ishizaki, A.; Jonas, D. M.; Lundeen, J. S.; McCusker, J. K.; Mukamel, S.; Ogilvie, J. P.; Olaya-Castro, A.; Ratner, M. A.; Spano, F. C.; Whaley, K. B.; Zhu, X. Using coherence to enhance function in chemical and biophysical systems. *Nature* **2017**, *543* (7647), 647−656.
(31) Bredas, J.-L.; Sargent, E. H.; Scholes, G. D. Photovoltaic concepts inspired by coherence effects in photosynthetic systems. *Nat. Mater.* **2017**, *16* (1), 35−44.
(32) Scholes, G. D.; Fleming, G. R.; Olaya-Castro, A.; van Grondelle, R. Lessons from nature about solar light harvesting. *Nat. Chem.* **2011**, *3* (10), 763−774.
(33) Biswas, S.; Kim, J.; Zhang, X.; Scholes, G. D. Coherent Two-Dimensional and Broadband Electronic Spectroscopies. *Chem. Rev.* **2022**, *122* (3), 4257−4321.
(34) Arsenault, E. A.; Yoneda, Y.; Iwai, M.; Niyogi, K. K.; Fleming, G. R. Vibronic mixing enables ultrafast energy flow in light-harvesting complex II. *Nat. Commun.* **2020**, *11* (1), 1460.
(35) Dean, J. C.; Mirkovic, T.; Toa, Z. S. D.; Oblinsky, D. G.; Scholes, G. D. Vibronic Enhancement of Algae Light Harvesting. *Chem* **2016**, *1* (6), 858−872.
(36) Halpin, A.; Johnson, P. J. M.; Tempelaar, R.; Murphy, R. S.; Knoester, J.; Jansen, T. L. C.; Miller, R. J. D. Two-dimensional spectroscopy of a molecular dimer unveils the effects of vibronic coupling on exciton coherences. *Nat. Chem.* **2014**, *6* (3), 196−201.
(37) Plenio, M. B.; Huelga, S. F. Dephasing-assisted transport: quantum networks and biomolecules. *New J. Phys.* **2008**, *10*, 113019.
(38) Song, Y.; Schubert, A.; Maret, E.; Burdick, R. K.; Dunietz, B. D.; Geva, E.; Ogilvie, J. P. Vibronic structure of photosynthetic pigments probed by polarized two-dimensional electronic spectroscopy and *ab initio* calculations. *Chem. Sci.* **2019**, *10* (35), 8143−8153.
(39) Son, M.; Pinnola, A.; Bassi, R.; Schlau-Cohen, G. S. The Electronic Structure of Lutein 2 Is Optimized for Light Harvesting in Plants. *Chem* **2019**, *5* (3), 575−584.
(40) Chenu, A.; Christensson, N.; Kauffmann, H. F.; Mancal, T. Enhancement of Vibronic and Ground-State Vibrational Coherences in 2D Spectra of Photosynthetic Complexes. *Sci. Rep.* **2013**, *3*, 2029.
(41) Abramavicius, D.; Voronine, D. V.; Mukamel, S. Unravelling coherent dynamics and energy dissipation in photosynthetic complexes by 2D spectroscopy. *Biophys. J.* **2008**, *94* (9), 3613−3619.
(42) Van Amerongen, H. V. L.; Van Grondelle, R.; Valkunas, L. *Photosynthetic Excitons*; World Scientific Publishing Co. Pte. Ltd.; Vol. *604*, 2000.
(43) Mohseni, M.; Rebentrost, P.; Lloyd, S.; Aspuru-Guzik, A. Environment-assisted quantum walks in photosynthetic energy transfer. *J. Chem. Phys.* **2008**, *129* (17), 174106.
(44) Rebentrost, P.; Mohseni, M.; Kassal, I.; Lloyd, S.; Aspuru-Guzik, A. Environment-assisted quantum transport. *New J. Phys.* **2009**, *11*, 033003.
(45) Rebentrost, P.; Mohseni, M.; Aspuru-Guzik, A. Role of Quantum Coherence and Environmental Fluctuations in Chromophoric Energy Transport. *J. Phys. Chem. B* **2009**, *113* (29), 9942−9947.
(46) Caruso, F.; Chin, A. W.; Datta, A.; Huelga, S. F.; Plenio, M. B. Highly efficient energy excitation transfer in light-harvesting complexes: The fundamental role of noise-assisted transport. *J. Chem. Phys.* **2009**, *131* (10), 105106.
(47) Panitchayangkoon, G.; Hayes, D.; Fransted, K. A.; Caram, J. R.; Harel, E.; Wen, J.; Blankenship, R. E.; Engel, G. S. Long-lived quantum coherence in photosynthetic complexes at physiological temperature. *Proc. Natl. Acad. Sci. U. S. A.* **2010**, *107* (29), 12766−12770.
(48) Womick, J. M.; Moran, A. M. Vibronic Enhancement of Exciton Sizes and Energy Transport in Photosynthetic Complexes. *J. Phys. Chem. B* **2011**, *115* (6), 1347−1356.
(49) Womick, J. M.; Moran, A. M. Exciton Coherence and Energy Transport in the Light-Harvesting Dimers of Allophycocyanin. *J. Phys. Chem. B* **2009**, *113* (48), 15747−15759.
(50) Maiuri, M.; Ostroumov, E. E.; Saer, R. G.; Blankenship, R. E.; Scholes, G. D. Coherent wavepackets in the Fenna-Matthews-Olson complex are robust to excitonic-structure perturbations caused by mutagenesis. *Nat. Chem.* **2018**, *10* (2), 177−183.
(51) Brixner, T.; Stenger, J.; Vaswani, H. M.; Cho, M.; Blankenship, R. E.; Fleming, G. R. Two-dimensional spectroscopy of electronic couplings in photosynthesis. *Nature* **2005**, *434* (7033), 625−628.
(52) Rolczynski, B. S.; Zheng, H.; Singh, V. P.; Navotnaya, P.; Ginzburg, A. R.; Caram, J. R.; Ashraf, K.; Gardiner, A. T.; Yeh, S.-H.; Kais, S.; Cogdell, R. J.; Engel, G. S. Correlated Protein Environments Drive Quantum Coherence Lifetimes in Photosynthetic Pigment-Protein Complexes. *Chem* **2018**, *4* (1), 138−149.
(53) Chin, A. W.; Huelga, S. F.; Plenio, M. B. Coherence and Decoherence in Biological Systems: Principles of Noise Assisted Transport and the Origin of Long-lived Coherences. *Philos. Trans A Math Phys. Eng.* **2012**, *370* (1972), 3638−3657.
(54) Lee, H.; Cheng, Y. C.; Fleming, G. R. Coherence dynamics in photosynthesis: Protein protection of excitonic coherence. *Science* **2007**, *316* (5830), 1462−1465.
(55) Rivera, E.; Montemayor, D.; Masia, M.; Coker, D. F. Influence of Site-Dependent Pigment-Protein Interactions on Excitation Energy Transfer in Photosynthetic Light Harvesting. *J. Phys. Chem. B* **2013**, *117* (18), 5510−5521.
(56) Olbrich, C.; Struempfer, J.; Schulten, K.; Kleinekathoefer, U. Theory and Simulation of the Environmental Effects on FMO Electronic Transitions. *J. Phys. Chem. Lett.* **2011**, *2* (14), 1771−1776.
(57) Duan, H. G.; Prokhorenko, V. I.; Cogdell, R. J.; Ashraf, K.; Stevens, A. L.; Thorwart, M.; Miller, R. J. D. Nature does not rely on long-lived electronic quantum coherence for photosynthetic energy transfer. *Proc. Natl. Acad. Sci. U. S. A.* **2017**, *114* (32), 8493−8498.
(58) Tiwari, V.; Peters, W. K.; Jonas, D. M. Electronic resonance with anticorrelated pigment vibrations drives photosynthetic energy transfer outside the adiabatic framework. *Proc. Natl. Acad. Sci. U.S.A.* **2013**, *110* (4), 1203−1208.
(59) Christensson, N.; Kauffmann, H. F.; Pullerits, T.; Mancal, T. Origin of Long-Lived Coherences in Light-Harvesting Complexes. *J. Phys. Chem. B* **2012**, *116* (25), 7449−7454.
(60) Jonas, D. M. Vibrational and Nonadiabatic Coherence in 2D Electronic Spectroscopy, the Jahn-Teller Effect, and Energy Transfer. *Annu. Rev. Phys. Chem.* **2018**, *69*, 327−352.
(61) Farrell, K. M.; Yang, N.; Zanni, M. T. A polarization scheme that resolves cross-peaks with transient absorption and eliminates diagonal peaks in 2D spectroscopy. *Proc. Natl. Acad. Sci. U.S.A.* **2022**, *119* (6), No. e2117398119.
(62) Read, E. L.; Engel, G. S.; Calhoun, T. R.; Mancal, T.; Ahn, T. K.; Blankenship, R. E.; Fleming, G. R. Cross-peak-specific two-dimensional electronic spectroscopy. *Proc. Natl. Acad. Sci. U.S.A.* **2007**, *104* (36), 14203−14208.
(63) Sohoni, S.; Wu, P.-J. E.; Shen, Q.; Lloyd, L. T.; MacGregor-Chatwin, C.; Hitchcock, A.; Engel, G. S. Resonant Vibrational Enhancement of Downhill Energy Transfer in the C-Phycocyanin Chromophore Dimer. *J. Phys. Chem. Lett.* **2024**, *15* (46), 11569−11576.

https://doi.org/10.1021/acs.jpcb.5c07333
J. Phys. Chem. B 2026, 130, 4017−4040

(64) Freixas, V. M.; Tretiak, S.; Makhov, D. V.; Shalashilin, D. V.; Fernandez-Alberti, S. Vibronic Quantum Beating between Electronic Excited States in a Heterodimer. *J. Phys. Chem. B* **2020**, *124* (19), 3992−4001.
(65) Chin, A. W.; Prior, J.; Rosenbach, R.; Caycedo-Soler, F.; Huelga, S. F.; Plenio, M. B. The role of non-equilibrium vibrational structures in electronic coherence and recoherence in pigment-protein complexes. *Nat. Phys.* **2013**, *9* (2), 113−118.
(66) Scholes, G. D.; Olaya-Castro, A.; Mukamel, S.; Kirrander, A.; Ni, K.-K.; Hedley, G. J.; Frank, N. L. The Quantum Information Science Challenge for Chemistry. *J. Phys. Chem. Lett.* **2025**, *16* (5), 1376−1396.
(67) Joo, T.; Albrecht, A. C. ELECTRONIC DEPHASING STUDIES OF MOLECULES IN SOLUTION AT ROOM-TEMPERATURE BY FEMTOSECOND DEGENERATE 4-WAVE-MIXING. *Chem. Phys.* **1993**, *176* (1), 233−247.
(68) Siwiak-Jaszek, S.; Olaya-Castro, A. Transient synchronisation and quantum coherence in a bio-inspired vibronic dimer. *Faraday Discuss.* **2019**, *216*, 38−56.
(69) Chin, A. W.; Huelga, S. F.; Plenio, M. B. Coherence and decoherence in biological systems: principles of noise-assisted transport and the origin of long-lived coherences. *Philos. Trans. R. Soc. A Math. Phys. Eng. Sci.* **2012**, *370* (1972), 3638−3657.
(70) Lee, H.; Cheng, Y.-C.; Fleming, G. R. Coherence dynamics in photosynthesis: Protein protection of excitonic coherence. *Science* **2007**, *316* (5830), 1462−1465.
(71) Olbrich, C.; Jansen, T. L. C.; Liebers, J.; Aghtar, M.; Struempfer, J.; Schulten, K.; Knoester, J.; Kleinekathoefer, U. From Atomistic Modeling to Excitation Transfer and Two-Dimensional Spectra of the FMO Light-Harvesting Complex. *J. Phys. Chem. B* **2011**, *115* (26), 8609−8621.
(72) Renger, T.; Klinger, A.; Steinecker, F.; Schmidt am Busch, M.; Numata, J.; Müh, F. Normal Mode Analysis of the Spectral Density of the Fenna-Matthews-Olson Light-Harvesting Protein: How the Protein Dissipates the Excess Energy of Excitons. *J. Phys. Chem. B* **2012**, *116* (50), 14565−14580.
(73) Siwiak-Jaszek, S.; Le, T. P.; Olaya-Castro, A. Synchronization phase as an indicator of persistent quantum correlations between subsystems. *Phys. Rev. A* **2020**, *102* (3), 032414.
(74) O'Reilly, E. J.; Olaya-Castro, A. Non-classicality of the molecular vibrations assisting exciton energy transfer at room temperature. *Nat. Commun.* **2014**, *5*, 3012.
(75) Cho, K. H.; Rhee, Y. M. Cooperation between Excitation Energy Transfer and Antisynchronously Coupled Vibrations. *J. Phys. Chem. B* **2021**, *125* (21), 5601−5610.
(76) Yan, Y. J.; Mukamel, S. FEMTOSECOND PUMP-PROBE SPECTROSCOPY OF POLYATOMIC-MOLECULES IN CONDENSED PHASES. *Phys. Rev. A:At., Mol., Opt. Phys.* **1990**, *41* (11), 6485−6504.
(77) Yan, Y. J.; Mukamel, S. ELECTRONIC DEPHASING, VIBRATIONAL-RELAXATION, AND SOLVENT FRICTION IN MOLECULAR NONLINEAR OPTICAL-LINE SHAPES. *J. Chem. Phys.* **1988**, *89* (8), 5160−5176.
(78) Tiwari, V.; Jonas, D. M. Electronic energy transfer through non-adiabatic vibrational-electronic resonance. II. 1D spectra for a dimer. *J. Chem. Phys.* **2018**, *148* (8), 084308.
(79) Glazer, A. N. Light guides: Directional energy transfer in a photosynthetic antenna. *J. Biol. Chem.* **1989**, *264* (1), 1−4.
(80) Womick, J. M.; Moran, A. M. Nature of Excited States and Relaxation Mechanisms in C-Phycocyanin. *J. Phys. Chem. B* **2009**, *113* (48), 15771.
(81) Zhang, J. M.; Shiu, Y. J.; Hayashi, M.; Liang, K. K.; Chang, C. H.; Gulbinas, V.; Yang, C. M.; Yang, T. S.; Wang, H. Z.; Chen, Y. T.; Lin, S. H. Investigations of ultrafast exciton dynamics in allophycocyanin trimer. *J. Phys. Chem. A* **2001**, *105* (39), 8878−8891.
(82) Edington, M. D.; Riter, R. E.; Beck, W. F. EVIDENCE FOR COHERENT ENERGY-TRANSFER IN ALLOPHYCOCYANIN TRIMERS. *J. Phys. Chem.* **1995**, *99* (43), 15699−15704.
(83) Riter, R. R.; Edington, M. D.; Reck, W. F. Protein-matrix solvation dynamics in the alpha subunit of C-phycocyanin. *J. Phys. Chem.* **1996**, *100* (33), 14198−14205.
(84) Yue, S.; Wang, Z.; Leng, X.; Zhu, R.-D.; Chen, H.-L.; Weng, Y.-X. Coupling of multi-vibrational modes in bacteriochlorophyll a in solution observed with 2D electronic spectroscopy. *Chem. Phys. Lett.* **2017**, *683*, 591−597.
(85) Fleming, G. R.; Cho, M. H. Chromophore-solvent dynamics. *Annu. Rev. Phys. Chem.* **1996**, *47*, 109−134.
(86) Tsubouchi, M.; Ishii, N.; Fujita, T.; Adachi, M.; Itakura, R. Dependence of energy relaxation and vibrational coherence on the location of light-harvesting chromoproteins in photosynthetic antenna protein complexes. *J. Chem. Phys.* **2025**, *162* (14), 145102.
(87) Rathbone, H. W.; Michie, K. A.; Landsberg, M. J.; Green, B. R.; Curmi, P. M. G. Scaffolding proteins guide the evolution of algal light harvesting antennas. *Nat. Commun.* **2021**, *12* (1), 1890.
(88) Wilk, K. E.; Harrop, S. J.; Jankova, L.; Edler, D.; Keenan, G.; Sharples, F.; Hiller, R. G.; Curmi, P. M. G. Evolution of a light-harvesting protein by addition of new subunits and rearrangement of conserved elements: Crystal structure of a cryptophyte phycoerythrin at 1.63-Å resolution. *Proc. Natl. Acad. Sci. U. S. A.* **1999**, *96* (16), 8901−8906.
(89) Maccoll, R.; Guardfriar, D.; Williams, E. C. SPECTROSCOPIC STUDIES ON PHYCOERYTHRIN 545, ITS BILINS, AND ITS ISOPROTEINS. *J. Lumin.* **1992**, *51* (1−3), 21−28.
(90) Wong, C. Y.; Alvey, R. M.; Turner, D. B.; Wilk, K. E.; Bryant, D. A.; Curmi, P. M. G.; Silbey, R. J.; Scholes, G. D. Electronic coherence lineshapes reveal hidden excitonic correlations in photosynthetic light harvesting. *Nat. Chem.* **2012**, *4* (5), 396−404.
(91) Collini, E.; Wong, C. Y.; Wilk, K. E.; Curmi, P. M. G.; Brumer, P.; Scholes, G. D. Coherently wired light-harvesting in photosynthetic marine algae at ambient temperature. *Nature* **2010**, *463* (7281), 644−U69.
(92) Cui, X.-Y.; Yan, Y.-J.; Wei, J.-H. Theoretical study on the exciton dynamics of coherent excitation energy transfer in the phycoerythrin 545 light-harvesting complex. *Chin. Phys. B* **2022**, *31* (1), 018201.
(93) Hossein-Nejad, H.; Curutchet, C.; Kubica, A.; Scholes, G. D. Delocalization-Enhanced Long-Range Energy Transfer between Cryptophyte Algae PE545 Antenna Proteins. *J. Phys. Chem. B* **2011**, *115* (18), 5243−5253.
(94) Aghtar, M.; Kleinekathoefer, U. Environmental coupling and population dynamics in the PE545 light-harvesting complex. *J. Lumin.* **2016**, *169*, 406−409.
(95) Doust, A. B.; Wilk, K. E.; Curmi, P.; Scholes, G. D. The photophysics of cryptophyte light-harvesting. *J. Photochem. Photobiol., A* **2006**, *184* (1−2), 1−17.
(96) Novoderezhkin, V. I.; Doust, A. B.; Curutchet, C.; Scholes, G. D.; van Grondelle, R. Excitation Dynamics in Phycoerythrin 545: Modeling of Steady-State Spectra and Transient Absorption with Modified Redfield Theory. *Biophys. J.* **2010**, *99* (2), 344−352.
(97) Andel, F.; Murphy, J. T.; Haas, J. A.; McDowell, M. T.; van der Hoef, I.; Lugtenburg, J.; Lagarias, J. C.; Mathies, R. A. Probing the photoreaction mechanism of phytochrome through analysis of resonance Raman vibrational spectra of recombinant analogues. *Biochemistry* **2000**, *39* (10), 2667−2676.
(98) Cogdell, R. J.; Gall, A.; Koehler, J. The architecture and function of the light-harvesting apparatus of purple bacteria:: from single molecules to in vivo membranes. *Q. Rev. Biophys.* **2006**, *39* (3), 227−324.
(99) David, L.; Prado, M.; Arteni, A. A.; Elmlund, D. A.; Blankenship, R. E.; Adir, N. Structural studies show energy transfer within stabilized phycobilisomes independent of the mode of rod-core assembly. *Biochim. Biophys. Acta, Bioenerg.* **2014**, *1837* (3), 385−395.
(100) Adir, N.; Dobrovetsky, Y.; Lerner, N. Structure of c-phycocyanin from the thermophilic cyanobacterium Synechococcus vulcanus at 2.5 Å: Structural implications for thermal stability in phycobilisome assembly. *J. Mol. Biol.* **2001**, *313* (1), 71−81.

https://doi.org/10.1021/acs.jpcb.5c07333
J. Phys. Chem. B 2026, 130, 4017−4040

(101) Sohoni, S.; Lloyd, L. T.; Hitchcock, A.; MacGregor-Chatwin, C.; Iwanicki, A.; Ghosh, I.; Shen, Q.; Hunter, C. N.; Engel, G. S. Phycobilisome's Exciton Transfer Efficiency Relies on an Energetic Funnel Driven by Chromophore-Linker Protein Interactions. *J. Am. Chem. Soc.* **2023**, *145* (21), 11659−11668.
(102) Sil, S.; Tilluck, R. W.; Mohan T M, N.; Leslie, C. H.; Rose, J. B.; Dominguez-Martin, M. A.; Lou, W.; Kerfeld, C. A.; Beck, W. F. Excitation energy transfer and vibronic coherence in intact phycobilisomes. *Nat. Chem.* **2022**, *14* (11), 1286−1294.
(103) Nield, J.; Rizkallah, P. J.; Barber, J.; Chayen, N. E. The 1.45 Å three-dimensional structure of C-phycocyanin from the thermophilic cyanobacterium Synechococcus elongatus. *J. Struct. Biol.* **2003**, *141* (2), 149−155.
(104) Schirmer, T.; Bode, W.; Huber, R. REFINED 3-DIMENSIONAL STRUCTURES OF 2 CYANOBACTERIAL C-PHYCOCYANINS AT 2.1 AND 2.5 A RESOLUTION - A COMMON PRINCIPLE OF PHYCOBILIN-PROTEIN INTERACTION. *J. Mol. Biol.* **1987**, *196* (3), 677−695.
(105) Brejc, K.; Ficner, R.; Huber, R.; Steinbacher, S. Isolation, crystallization, crystal structure analysis and refinement of allophycocyanin from the cyanobacterium Spirulina platensis at 2.3 A resolution. *J.mol.biol* **1995**, *249* (2), 424−440.
(106) Förster, T. Intermolecular energy migration and fluorescence. *Ann. Phys.* **1948**, *437*, 55−75.
(107) Fox, K. F.; Balevicius, V., Jr.; Chmeliov, J.; Valkunas, L.; Ruban, A. V.; Duffy, C. D. P. The carotenoid pathway: what is important for excitation quenching in plant antenna complexes? *Phys. Chem. Chem. Phys.* **2017**, *19* (34), 22957−22968.
(108) You, Z. Q.; Hsu, C. P. Theory and calculation for the electronic coupling in excitation energy transfer. *Int. J. Quantum Chem.* **2014**, *114* (2), 102−115.
(109) Debreczeny, M. P.; Sauer, K.; Zhou, J. H.; Bryant, D. A. MONOMERIC C-PHYCOCYANIN AT ROOM-TEMPERATURE AND 77-K - RESOLUTION OF THE ABSORPTION AND FLUORESCENCE-SPECTRA OF THE INDIVIDUAL CHROMOPHORES AND THE ENERGY-TRANSFER RATE CONSTANTS. *J. Phys. Chem.* **1993**, *97* (38), 9852−9862.
(110) Collini, E. Spectroscopic signatures of quantum-coherent energy transfer. *Chem. Soc. Rev.* **2013**, *42* (12), 4932−4947.
(111) Zhao, J.; Weng, Y.; Zheng, Z. The Structure and Mechanism of Energy Transfer in Phycobilisomes. *Annu. Rev. Microbiol.* **2025**, *79* (1), 263−295.
(112) Ruban, A. V.; Wilson, S. The Mechanism of Non-Photochemical Quenching in Plants: Localization and Driving Forces. *Plant Cell Physiol.* **2021**, *62* (7), 1063−1072.
(113) Ruban, A. V. Light harvesting control in plants. *FEBS Lett.* **2018**, *592* (18), 3030−3039.
(114) Murchie, E. H.; Niyogi, K. K. Manipulation of photoprotection to improve plant photosynthesis. *Plant Physiol.* **2011**, *155* (1), 86−92.
(115) Li, X. P.; Gilmore, A. M.; Caffarri, S.; Bassi, R.; Golan, T.; Kramer, D.; Niyogi, K. K. Regulation of Photosynthetic Light Harvesting Involves Intrathylakoid Lumen pH Sensing by the PsbS Protein. *J. Biol. Chem.* **2004**, *279* (22), 22866−22874.
(116) Horton, P.; Ruban, A. V.; Walters, R. G. Regulation of light harvesting in green plants. *Annu. Rev. Plant Physiol. Plant Mol. Biol.* **1996**, *47*, 655−684.
(117) Zheng, M.; Pang, X.; Chen, M.; Tian, L. Ultrafast energy quenching mechanism of LHCSR3-dependent photoprotection in Chlamydomonas. *Nat. Commun.* **2024**, *15* (1), 4437.
(118) Pinnola, A.; Bassi, R. Molecular mechanisms involved in plant photoprotection. *Biochem. Soc. Trans.* **2018**, *46* (2), 467−482.
(119) Horton, P.; Wentworth, M.; Ruban, A. Control of the light harvesting function of chloroplast membranes: The LHCII-aggregation model for non-photochemical quenching. *FEBS Lett.* **2005**, *579* (20), 4201−4206.
(120) Horton, P.; Ruban, A. V.; Wentworth, M. Allosteric regulation of the light-harvesting system of photosystem II. *Phil. Trans. Roy. Soc. Lond. B Biol. Sci.* **2000**, *355* (1402), 1361−1370.
(121) Bassi, R.; Caffarri, S. Lhc proteins and the regulation of photosynthetic light harvesting function by xanthophylls. *Photosynth. Res.* **2000**, *64* (2−3), 243−256.
(122) Ruban, A. V.; Johnson, M. P.; Duffy, C. D. P. The photoprotective molecular switch in the photosystem II antenna. *Biochim. Biophys. Acta, Bioenerg.* **2012**, *1817* (1), 167−181.
(123) Wilson, S.; Clarke, C. D.; Carbajal, M. A.; Buccafusca, R.; Fleck, R. A.; Daskalakis, V.; Ruban, A. V. Hydrophobic Mismatch in the Thylakoid Membrane Regulates Photosynthetic Light Harvesting. *J. Am. Chem. Soc.* **2024**, *146* (21), 14905−14914.
(124) Ruban, A. V. Unveiling the atomic-scale transition between light harvesting and photoprotective states in plant photosynthesis. *Sci. China:Chem.* **2024**, *67* (5), 1375−1377.
(125) van Amerongen, H.; Croce, R. Non-Photochemical Quenching in Plants: Mechanisms and Mysteries. *Plant Cell* **2025**, *37* (11), koaf240.
(126) Duffy, C. D. P.; Chmeliov, J.; Macernis, M.; Sulskus, J.; Valkunas, L.; Ruban, A. V. Modeling of Fluorescence Quenching by Lutein in the Plant Light-Harvesting Complex LHCII. *J. Phys. Chem. B* **2013**, *117* (38), 10974−10986.
(127) Ruban, A. V.; Berera, R.; Ilioaia, C.; van Stokkum, I. H. M.; Kennis, J. T. M.; Pascal, A. A.; van Amerongen, H.; Robert, B.; Horton, P.; van Grondelle, R. Identification of a mechanism of photoprotective energy dissipation in higher plants. *Nature* **2007**, *450* (7169), 575−U22.
(128) Sardar, S.; Caferri, R.; Camargo, F. V. A.; Pamos Serrano, J.; Ghezzi, A.; Capaldi, S.; Dall'Osto, L.; Bassi, R.; D'Andrea, C.; Cerullo, G. Molecular mechanisms of light harvesting in the minor antenna CP29 in near-native membrane lipidic environment. *J. Chem. Phys.* **2022**, *156* (20), 205101.
(129) Mascoli, V.; Liguori, N.; Xu, P.; Roy, L. M.; van Stokkum, I. H. M.; Croce, R. Capturing the Quenching Mechanism of Light-Harvesting Complexes of Plants by Zooming in on the Ensemble. *Chem* **2019**, *5* (11), 2900−2912.
(130) Liguori, N.; Xu, P.; van Stokkum, I. H. M.; van Oort, B.; Lu, Y.; Karcher, D.; Bock, R.; Croce, R. Different carotenoid conformations have distinct functions in light-harvesting regulation in plants. *Nat. Commun.* **2017**, *8* (1), 1994.
(131) Wahadoszamen, M.; Berera, R.; Ara, A. M.; Romero, E.; van Grondelle, R. Identification of two emitting sites in the dissipative state of the major light harvesting antenna. *Phys. Chem. Chem. Phys.* **2012**, *14* (2), 759−766.
(132) Ahn, T. K.; Avenson, T. J.; Ballottari, M.; Cheng, Y.-C.; Niyogi, K. K.; Bassi, R.; Fleming, G. R. Architecture of a charge-transfer state regulating light harvesting in a plant antenna protein. *Science* **2008**, *320* (5877), 794−797.
(133) Holt, N. E.; Zigmantas, D.; Valkunas, L.; Li, X. P.; Niyogi, K. K.; Fleming, G. R. Carotenoid cation formation and the regulation of photosynthetic light harvesting. *Science* **2005**, *307* (5708), 433−436.
(134) Cupellini, L.; Calvani, D.; Jacquemin, D.; Mennucci, B. Charge transfer from the carotenoid can quench chlorophyll excitation in antenna complexes of plants. *Nat. Commun.* **2020**, *11* (1), 662.
(135) Liu, Z. F.; Yan, H. C.; Wang, K. B.; Kuang, T. Y.; Zhang, J. P.; Gui, L. L.; An, X. M.; Chang, W. R. Crystal structure of spinach major light-harvesting complex at 2.72 angstrom resolution. *Nature* **2004**, *428* (6980), 287−292.
(136) Tang, Y.; Wen, X.; Lu, Q.; Yang, Z.; Cheng, Z.; Lu, C. Heat stress induces an aggregation of the light-harvesting complex of photosystem II in spinach plants. *Plant Physiol.* **2007**, *143* (2), 629−638.
(137) Wentworth, M.; Ruban, A. V.; Horton, P. Thermodynamic investigation into the mechanism of the chlorophyll fluorescence quenching in isolated photosystem II light-harvesting complexes. *J. Biol. Chem.* **2003**, *278* (24), 21845−21850.
(138) Barzda, V.; Istokovics, A.; Simidjiev, I.; Garab, G. Structural flexibility of chiral macroaggregates of light-harvesting chlorophyll a/b pigment-protein complexes. Light-induced reversible structural

https://doi.org/10.1021/acs.jpcb.5c07333
J. Phys. Chem. B 2026, 130, 4017−4040

changes associated with energy dissipation. *Biochemistry* **1996**, *35* (27), 8981−8985.
(139) Ruan, M.; Xu, Y.; Liao, G.; Wang, Z.; Chen, H.; Weng, Y. Investigation of Transient Temperature Rising of Light-Harvesting Complex II by Nonradiative Heat Dissipation at the Protein Level. *J. Phys. Chem. Lett.* **2025**, *16* (1), 308−316.
(140) Ide, J. P.; Klug, D. R.; Kuhlbrandt, W.; Giorgi, L. B.; Porter, G. THE STATE OF DETERGENT SOLUBILIZED LIGHT-HARVESTING CHLOROPHYLL-A/B PROTEIN COMPLEX AS MONITORED BY PICOSECOND TIME-RESOLVED FLUORESCENCE AND CIRCULAR-DICHROISM. *Biochim. Biophys. Acta* **1987**, *893* (2), 349−364.
(141) van Amerongen, H.; van Grondelle, R. Understanding the energy transfer function of LHCII, the major light-harvesting complex of green plants. *J. Phys. Chem. B* **2001**, *105* (3), 604−617.
(142) Garab, G. *Photosynthesis: Mechanisms and Effects*; Springer, 1998.
(143) Koyama, Y.; Kakitani, Y.; Miki, T.; Christiana, R.; Nagae, H. Excited-State Dynamics of Overlapped Optically-Allowed 1Bu+ and Optically-Forbidden 1Bu- or 3Ag- Vibronic Levels of Carotenoids: Possible Roles in the Light-Harvesting Function. *Int. J. Mol. Sci.* **2010**, *11* (4), 1888−1929.
(144) Li, H.; Wang, Y.; Ye, M.; Li, S.; Li, D.; Ren, H.; Wang, M.; Du, L.; Li, H.; Veglia, G.; Gao, J.; Weng, Y. Dynamical and allosteric regulation of photoprotection in light harvesting complex II. *Sci. China Chem.* **2020**, *63* (8), 1121−1133.
(145) Li, D.; Li, Y.; Li, H.; Wu, X.; Yu, Q.; Weng, Y.; Ho, A. Q-switched YAG laser assisted nanosecond time-resolved T-jump transient mid-IR absorbance spectroscopy with high sensitivity. *Rev. Sci. Instrum.* **2015**, *86* (5), 053105.
(146) Lu, Y.; Gao, J. Multistate Density Functional Theory: Theory, Methods, and Applications. *Wiley Interdiscip. Rev. Comput. Mol. Sci.* **2025**, *15* (5), No. e70043.
(147) Daskalakis, V.; Maity, S.; Hart, C. L.; Stergiannakos, T.; Duffy, C. D. P.; Kleinekathofer, U. Structural Basis for Allosteric Regulation in the Major Antenna Trimer of Photosystem II. *J. Phys. Chem. B* **2019**, *123* (45), 9609−9615.
(148) Madjet, M. E. A.; Müh, F.; Renger, T. Thomas Renger Deciphering the influence of short-range electronic couplings on optical properties of molecular dimers: application to "special pairs" in photosynthesis. *J. Phys. Chem. B.* **2009**, *113* (37), 12603−12614.
(149) Saccon, F.; Durchan, M.; Polívka, T.; Ruban, A. V. The robustness of the terminal emitter site in major LHCII complexes controls xanthophyll function during photoprotection. *Photochem. Photobiol. Sci.* **2020**, *19* (10), 1308−1318.
(150) Olaya-Castro, A.; Scholes, G. D. Energy transfer from Forster-Dexter theory to quantum coherent light-harvesting. *Int. Rev. Phys. Chem.* **2011**, *30* (1), 49−77.
(151) Zhu, X. G.; Ort, D. R.; Whitmarsh, J.; Long, S. P. The slow reversibility of photosystem II thermal energy dissipation on transfer from high to low light may cause large losses in carbon gain by crop canopies: a theoretical analysis. *J. Exp. Bot.* **2004**, *55* (400), 1167−1175.
(152) Adams, D. *Non-photochemical quenching and energy dissipation in Plants, Algae and Cyanobacteria*; Springer: Netherlands, 2014.
(153) Jahns, P.; Latowski, D.; Strzalka, K. Mechanism and regulation of the violaxanthin cycle: The role of antenna proteins and membrane lipids. *Biochim. Biophys. Acta, Bioenerg.* **2009**, *1787* (1), 3−14.
(154) Murchie, E. H.; Ruban, A. V. Dynamic non-photochemical quenching in plants: from molecular mechanism to productivity. *Plant J.* **2020**, *101* (4), 885−896.
(155) De Souza, A. P.; Burgess, S. J.; Doran, L.; Hansen, J.; Manukyan, L.; Maryn, N.; Gotarkar, D.; Leonelli, L.; Niyogi, K. K.; Long, S. P. Soybean photosynthesis and crop yield are improved by accelerating recovery from photoprotection. *Science* **2022**, *377* (6608), 851−854.
(156) Kromdijk, J.; Glowacka, K.; Leonelli, L.; Gabilly, S. T.; Iwai, M.; Niyogi, K. K.; Long, S. P. Improving photosynthesis and crop productivity by accelerating recovery from photoprotection. *Science* **2016**, *354* (6314), 857−861.
(157) Lehretz, G. G.; Schneider, A.; Leister, D.; Sonnewald, U. High non-photochemical quenching of VPZ transgenic potato plants limits CO2 assimilation under high light conditions and reduces tuber yield under fluctuating light. *J. Integr. Plant Biol.* **2022**, *64* (9), 1821−1832.
(158) Garcia-Molina, A.; Leister, D. Accelerated relaxation of photoprotection impairs biomass accumulation in Arabidopsis. *Nat. Plants* **2020**, *6* (1), 9−12.
(159) Fleming, G. R.; Grondelle, R. Femtosecond spectroscopy of photosynthetic light-harvesting systems. *Curr. Opin. Struct. Biol.* **1997**, *7* (5), 738−748.
(160) Pullerits, T.; Sundström, V. Photosynthetic light-harvesting pigment-protein complexes: toward understanding how and why. *Acc. Chem. Res.* **1996**, *29* (8), 381−389.
(161) van Grondelle, R.; Dekker, J. P.; Gillbro, T.; Sundstrom, V. Energy transfer and trapping in photosynthesis. *Biochim. Biophys. Acta, Bioenerg.* **1994**, *1187* (1), 1−65.
(162) Jang, S.; Rivera, E.; Montemayor, D. Molecular Level Design Principle behind Optimal Sizes of Photosynthetic LH2 Complex: Taming Disorder through Cooperation of Hydrogen Bonding and Quantum Delocalization. *J. Phys. Chem. Lett.* **2015**, *6* (6), 928−934.
(163) Freer, A.; Prince, S.; Sauer, K.; Papiz, M.; Lawless, A. H.; McDermott, G.; Cogdell, R.; Isaacs, N. W. Pigment-pigment interactions and energy transfer in the antenna complex of the photosynthetic bacterium Rhodopseudomonas acidophile. *Structure* **1996**, *4* (4), 449−462.
(164) McDermott, G.; Prince, S.; Freer, A.; Hawthornthwaite-Lawless, A.; Papiz, M.; Cogdell, R.; Isaacs, N. Crystal structure of an integral membrane light-harvesting complex from photosynthetic bacteria. *Nature* **1995**, *374* (6522), 517−521.
(165) Hu, X. C.; Schulten, K. How nature harvests sunlight. *Phys. Today* **1997**, *50* (8), 28−34.
(166) Matsushita, M.; Ketelaars, M.; Van Oijen, A.; Köhler, J.; Aartsma, T.; Schmidt, J. Spectroscopy on the B850 band of individual light-harvesting 2 complexes of Rhodopseudomonas acidophila II. Exciton states of an elliptically deformed ring aggregate. *Biophys. J.* **2001**, *80* (3), 1604−1614.
(167) Ketelaars, M.; Van Oijen, A.; Matsushita, M.; Köhler, J.; Schmidt, J.; Aartsma, T. Spectroscopy on the B850 band of individual light-harvesting 2 complexes of Rhodopseudomonas acidophila I. Experiments and Monte Carlo simulations. *Biophys. J.* **2001**, *80* (3), 1591−1603.
(168) Bopp, M. A.; Sytnik, A.; Howard, T. D.; Cogdell, R. J.; Hochstrasser, R. M. The dynamics of structural deformations of immobilized single light-harvesting complexes. *Proc. Natl. Acad. Sci. U. S. A.* **1999**, *96* (20), 11271−11276.
(169) Hong, X. G.; Weng, Y. X.; Li, M. Determination of the topological shape of integral membrane protein light-harvesting complex LH2 from photosynthetic bacteria in the detergent solution by small-angle X-ray scattering. *Biophys. J.* **2004**, *86* (2), 1082−1088.
(170) Mostovoy, M. V.; Knoester, J. Statistics of optical spectra from single-ring aggregates and its application to LH2. *J. Phys. Chem. B* **2000**, *104* (51), 12355−12364.
(171) van Grondelle, R.; Novoderezhkin, V. Dynamics of excitation energy transfer in the LH1 and LH2 light-harvesting complexes of photosynthetic bacteria. *Biochemistry* **2001**, *40* (50), 15057−15068.
(172) Sundström, V.; Pullerits, T.; van Grondelle, R. Photosynthetic light-harvesting: reconciling dynamics and structure of purple bacterial LH2 reveals function of photosynthetic unit. *J. Phys. Chem. B* **1999**, *103* (13), 2327−2346.
(173) van Oijen, A. M.; Ketelaars, M.; Köhler, J.; Aartsma, T. J.; Schmidt, J. Unraveling the electronic structure of individual photosynthetic pigment-protein complexes. *Science* **1999**, *285* (5426), 400−402.
(174) Cupellini, L.; Caprasecca, S.; Guido, C. A.; Mueh, F.; Renger, T.; Mennucci, B. Coupling to Charge Transfer States is the Key to Modulate the Optical Bands for Efficient Light Harvesting in Purple Bacteria. *J. Phys. Chem. Lett.* **2018**, *9* (23), 6892−6899.

https://doi.org/10.1021/acs.jpcb.5c07333
J. Phys. Chem. B 2026, 130, 4017−4040

(175) Cupellini, L.; Jurinovich, S.; Campetella, M.; Caprasecca, S.; Guido, C. A.; Kelly, S. M.; Gardiner, A. T.; Cogdell, R.; Mennucci, B. An Ab Initio Description of the Excitonic Properties of LH2 and Their Temperature Dependence. *J. Phys. Chem. B* **2016**, *120* (44), 11348−11359.
(176) Jang, S.; Silbey, R. J.; Kunz, R.; Hofmann, C.; Koehler, J. Is There Elliptic Distortion in the Light Harvesting Complex 2 of Purple Bacteria? *J. Phys. Chem. B* **2011**, *115* (44), 12947−12953.
(177) Du, L.-C.; Huang, Y.-F.; Ren, B.; Weng, Y.-X. Photosynthetic Bacterial Light-Harvesting Antenna Complexes Adsorbed on Silica Nanoparticles Revealed by Silica Shell-Isolated Au Nanoparticle-Enhanced Raman Spectroscopy. *J. Phys. Chem. C* **2012**, *116* (12), 6993−6999.
(178) Ogren, J. I.; Tong, A. L.; Gordon, S. C.; Chenu, A.; Lu, Y.; Blankenship, R. E.; Cao, J.; Schlau-Cohen, G. S. Impact of the lipid bilayer on energy transfer kinetics in the photosynthetic protein LH2. *Chem. Sci.* **2018**, *9* (12), 3095−3104.
(179) Singharoy, A.; Maffeo, C.; Delgado-Magnero, K. H.; Swainsbury, D. J. K.; Sener, M.; Kleinekathoefer, U.; Vant, J. W.; Nguyen, J.; Hitchcock, A.; Isralewitz, B.; Teo, I.; Chandler, D. E.; Stone, J. E.; Phillips, J. C.; Pogorelov, T. V.; Mallus, M. I.; Chipot, C.; Luthey-Schulten, Z.; Tieleman, D. P.; Hunter, C. N.; Tajkhorshid, E.; Aksimentiev, A.; Schulten, K. Atoms to Phenotypes: Molecular Design Principles of Cellular Energy Metabolism. *Cell* **2019**, *179* (5), 1098−1111.
(180) Shi, Y.-R.; Ye, M.-P.; Du, L.-C.; Weng, Y.-X. Experimental Determination of Particle Size-Dependent Surface Charge Density for Silica Nanospheres. *J. Phys. Chem. C* **2018**, *122* (41), 23764−23771.
(181) Panc, V. *Theories of elastic plates*; Springer, 1975.
(182) Chu, Q. J.; Weng, Y. X. Structure-dependent wavelike energy transfer on pigment rings of individual light-harvesting-2 complexes from photosynthetic bacteria. *Phys. Rev. E:Stat., Nonlinear, Soft Matter Phys.* **2010**, *81* (4), 041917.
(183) Sener, M.; Hsin, J.; Trabuco, L. G.; Villa, E.; Qian, P.; Hunter, C. N.; Schulten, K. Structural model and excitonic properties of the dimeric RC-LH1-PufX complex from Rhodobacter sphaeroides. *Chem. Phys.* **2009**, *357* (1−3), 188−197.
(184) Chu, Q. J.; Yin, H. W.; Weng, Y. X. Coherent excitons at different orientation arrangements of local transition dipole moments in circular light-harvesting complexes. *Chin. Phys.* **2007**, *16* (10), 3052−3058.
(185) Hu, X.; Ritz, T.; Damjanovic, A.; Schulten, K. Pigment organization and transfer of electronic excitation in the photosynthetic unit of purple bacteria. *J. Phys. Chem. B* **1997**, *101* (19), 3854−3871.
(186) Zhang, Y.; Liu, H.; Weng, Y. Theoretical and Experimental Investigation of the Electronic Propensity Rule: A Linear Relationship between Radiative and Nonradiative Decay Rates of Molecules. *J. Phys. Chem. Lett.* **2023**, *14* (18), 4151−4157.
(187) Chandler, D. E.; Gumbart, J.; Stack, J. D.; Chipot, C.; Schulten, K. Membrane Curvature Induced by Aggregates of LH2s and Monomeric LH1s. *Biophys. J.* **2009**, *97* (11), 2978−2984.
(188) Tutkus, M.; Chmeliov, J.; Trinkunas, G.; Akhtar, P.; Lambrev, P. H.; Valkunas, L. Aggregation-related quenching of LHCII fluorescence in liposomes revealed by single-molecule spectroscopy. *J. Photochem. Photobiol., B* **2021**, *218*, 112174.
(189) Akhtar, P.; Dorogi, M.; Pawlak, K.; Kovacs, L.; Bota, A.; Kiss, T.; Garab, G.; Lambrev, P. H. Pigment Interactions in Light-harvesting Complex II in Different Molecular Environments. *J. Biol. Chem.* **2015**, *290* (8), 4877−4886.
(190) Bennett, C. H.; DiVincenzo, D. P. Quantum information and computation. *Nature* **2000**, *404* (6775), 247−255.

https://doi.org/10.1021/acs.jpcb.5c07333
J. Phys. Chem. B 2026, 130, 4017−4040